Budapest University of Technology and Economics
Department of Applied Mechanics

University of BRISTOL
Department of Engineering Mathematics

A study of the milled surface in the dynamics of milling

Author: **Dániel Bachrathy**
fifth year student
Budapest University of Technology and Economics

Supervisor: **Martin Homer**
lecturer
University of Bristol

Dave Barton
postgraduate student
University of Bristol

Advisor: **Gábor Stépán**
professor
Budapest University of Technology and Economics

Bristol, 2006

Table of contents

Acknowledgement

First of all, I thank to Gábor Stépán who inspired me and made me like mechanics. I also thank very much to Martin Homer for his supervision and corrections and to Dave Barton for his help in numerics. I am very grateful to Zoltán Dombóvári, Gábor Orosz and Róbert Szalai who made my life in Bristol so vivid. I acknowledge the support of my whole family who made my trip possible to the UK. Finally, I greatly thank to my fiancée, Tímea Gelencsér whose love helped me to go through all difficulties.

1. Introduction

Milling is a commonly used process in metal work, where the material is removed by the edge of a rotating tool. The technological parameters like the spin speed and the feed motions are limited mostly by the quality of the tool. Nowadays tools have a special coating or are made with inserts (figure 1). These tools can work properly in extreme condition.

Figure 1: Tool with coating and with inserts [16].

Thus very large spin speed and material removal rates can be achieved. This kind of process is known as high speed milling (HSM), HSM is becoming common in more and more sectors of industry, such as aerospace manufacturing. With this process a complex work-piece can be made in a short time. HSM technology is not cheap, but savings can be achieved by reducing the outlay of the assembling. By creating a large and complex part form a single work-piece, even 90% of the material can be removed during the milling process. That is why it is important to use a large material removal rate, whilst we also need good surface quality and geometric precision.

A good surface quality often cannot be achieved due to instability phenomenon such as regenerative-chatter. In the case of chatter, the tool has a large vibration relative to the work-piece, which causes unacceptable surface quality, overload of the machine-tool, rapid tool wear and noise. Thus chatter is unacceptable during the milling process. This kind of vibration is caused by a time delay effect through the cutting force. During the material

removal process the chip thickness depends on the actual position of the cutting edge and on the surface pattern which was formed by the edge path in the previous material removal step.

The description of this behaviour leads to models of HSM characterised by delayed differential equation (DDE). General description of DDEs can be found in [19]. The simplest type of a DDE is given by

$$\mathbf{y}'(t) = \mathbf{f}\big(t, \mathbf{y}(t), \mathbf{y}(t+\theta)\big), \qquad \theta \in \left[-\tau_{\max}, 0\right]. \tag{1}$$

Most models for milling process have a discrete time delay, but more sophisticated model can be found in [18] which use a functional DDE for mathematical model. To describe some non-linear behaviour of the process neutral DDE might be needed. The general form of a neutral DDE is given by

$$\mathbf{y}'(t) = \mathbf{f}\big(t, \mathbf{y}(t), \mathbf{y}(t+\theta), \mathbf{y}'(t+\theta)\big), \qquad \theta \in \left[-\tau_{\max}, 0\right]. \tag{2}$$

To solve a delayed differential equation we need an initial function on $t \in \left[-\tau_{\max}, 0\right]$ time interval.

The stability investigation must be made in an infinite dimensional phase space due to the time delay. The solutions for different type of DDE can be found in [20]. Closed form for stability boundaries cannot be made for DDE, expect some trivial case. That is why several numerical and semi-analytical method which change the DDE into a different form.

The semi-discretization method was described in [3], which approximates the DDE with a series of ODEs.

Computer program have also be written to solve some classes of DDEs and continue their solutions, such as DDE-BIFTOOL [10], and PDDE-CONT [9].

One of the first validations of the time delayed mathematical model was made by [6]. In this paper the quasi-periodic motion and the stability of the milling process were determined theoretically and by measurement. The authors found that the stability chart, which is a graph of the regions of stable solutions in parameter space (typical parameters are axial immersion

and the spin speed), has the same 'lobe-structure' as typically predicted by the time delayed models. Later, more complex models of the stability of the cutting process were investigated, such as interrupted turning [12]. This paper used a non-autonomous DDE to describe the cutting process. They found and improved theoretically the existence of the parametrically induced flip bifurcation lenses (islands), where periodic chatter occurs. The phenomenon of the periodic chatter was founded by measurement for milling in [2].

All the above mentioned studies used models of HSM with straight edged tool. Investigation for helical tool can be found e.g. in [11] and [17]. In these papers the helical tool was treated as a series of straight edged tools. In this case the edge is not a continuous curve. Stability investigations were made for a tool with a continuous helical edge in [13], where the flip lenses induced by the helical edge were described. In this paper the mathematical model was also validated by experimental results.

A periodic time delay ($\theta(t) = \theta(t+\tau)$) which is caused by the trochoidal tooth path of the cutting edge was taken into consideration in [7]. A model for state dependent delay ($\theta(\mathbf{y}(t))$) can be found in [8], which describes the turning process.

The aim of most articles to determine the stability boundaries of the cutting process. In most cases the forced excited motion is neglected or assumed to be small. However, in those regions where there is no self-excited vibration, the system is susceptible to large forced excited vibrations. In spite of this fact, there is much less investigation of the surface quality as the stability boundaries, and these models are not as well described. A description of milled surface generation for time domain simulation can be found in [5]. The method uses a model with a straight edged-tool. The same method was also used in [15], where the surface properties were determined over a stability chart. They found that both the surface location error (SLE), which is the distance between the desired and the milled surface, and the surface quality are large in the unstable region, and also significant in those regions where the ratio of the natural frequency of the system and the angular velocity is close to an integer.

The same phenomenon was shown in [1]. In this paper the periodic motions of the tool edge were calculated analytically. The surface location error was calculated from the edge path.

The main aim of this thesis is to predict the surface quality of the milled surface and describe how the measures of the surface quality vary as parameters of the model are changed.

First we investigated a two degree of freedom model with straight edged tool. We created the equations of motion of the system and calculated the stability chart using a semi-discretization

method. We checked our result with a different method by using the numerical calculation of a Matlab package called DDE-BIFTOOL, and found very good agreement. In the stable region of the stability chart we examined the behaviour of the transient motion. We found that there are special regions where it dies out much faster. Then we calculated the forced excited vibration of the tool both analytical, and with time domain simulation. We generated the surface of the particular solution of the tool motion, and described the calculation of the surface properties, such as surface location error and surface quality.

Secondly we extended our description to be able to describe a helical tool. We described the helical edges as a continuous line and calculated the exact excitation force of the helical tool. We calculated the stability chart with a semi-discretization method and found helix-induced flip lenses. We calculated the periodic motion of the tool by using a truncated Fourier series of the excitation. We generate the milled surface from the edge path, which is a two dimensional surface without regularity. We described the surface properties with the commonly used surface location error and surface quality, and introduced a new surface property, the surface waviness, which describes the deflections of the surface in the direction of the tool axis. This property is always zero for a straight-edged tool, but it can be of the same size as SLE for a tool with a small helix pitch.

Thirdly we described the effect of the technical parameters both on the stability and on surface properties in the models above. Our calculations supported the results of practical experiments, that larger axial immersion can be achieved by using small radial immersion and a tool with a few teeth.

We also found other advantages of helical tools: we can use a larger axial immersion at special angular velocities that cannot be used in case of straight edged tool. At these spin speed the system is close to resonance, which causes poor surface properties with a straight edged tool, while in the case of a helical tool we can achieve good surface properties by using a particular range of axial immersion.

Finally we propose a more accurate model to describe the chip thickness, which considers the vibration of the tool. We found a new type of stability loss, called a fold bifurcation, and regions in which there are multiple stable attractors.

2. Models

Several models can be used to understand the milling process. The model usually contains three main parts. The first describes the properties of the machine-tool, the second the function of the cutting force, and the third the description of the cutting process.

2.1. Machine-tool

The most important requirement of the machine-tool model is to describe the relation between the tool and the work-piece. They can be in relative motion, caused by a flexible tool, non-rigid holder or soft work-piece. The motion can be examined by a modal analysis. The motions have several modes and eigenfrequencies which can be measured; in most cases the first few modes are the most important. We can make a simple model which has similar behaviour. It can be described by the mass ($\mathbf{M}$), damping ($\mathbf{K}$) and the stiffness ($\mathbf{S}$) matrices, and will have as many degrees of freedom (DoF) as the number of eigenfrequencies we use.

Most of the articles [1, 2, 4, 7] use one or two DoF models, because in that case the calculation is much simpler and it gives a qualified description of the behaviour of the milling process. In these models either the tool or the work-pieces is flexible.

Typically we use the first two eigenfrequencies; there is no theoretical barrier to using more but it becomes more difficult to determine the modal matrices.

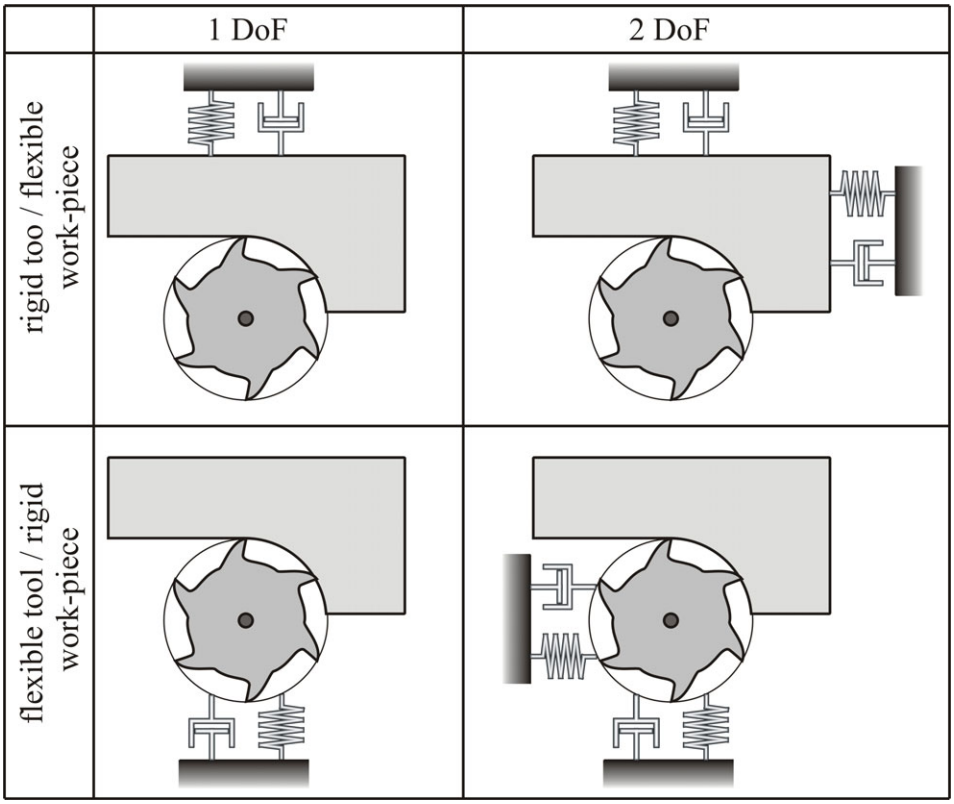

Table 1: Common used model for milling process

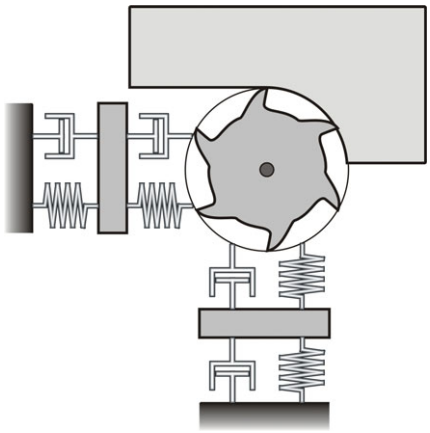

Figure 2: Model with four degrees of freedom.

In this report, we consider two different tools: with straight or helical edges. In the case of straight edges we can use a two dimensional (planar) model, while for the helical-edged tool we must use three spatial dimensions. In spite of the fact that most tools have helical edges we can approximate its behaviours with a straight-edged model if the axial immersion (*w*, shown in figure 4) of the tool is small (see figure 3).

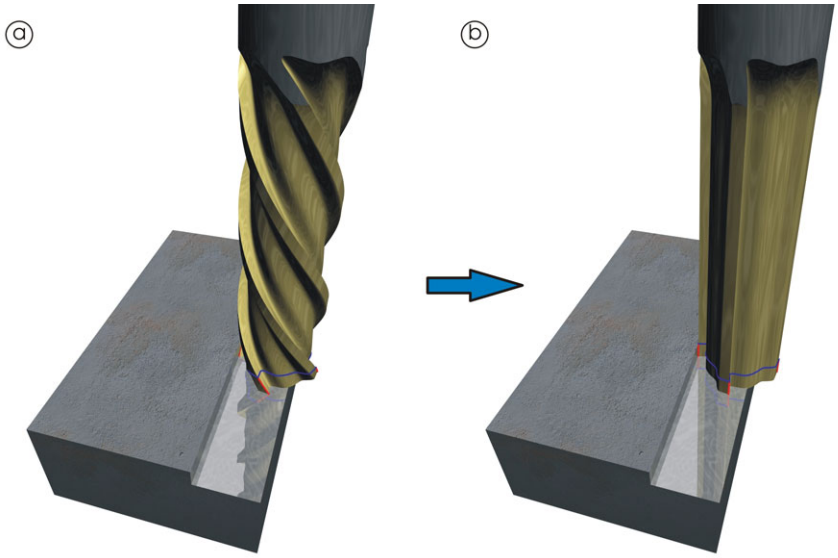

Figure 3: Helical edges (a) approximated with straight edges (b).

2.2. Cutting force

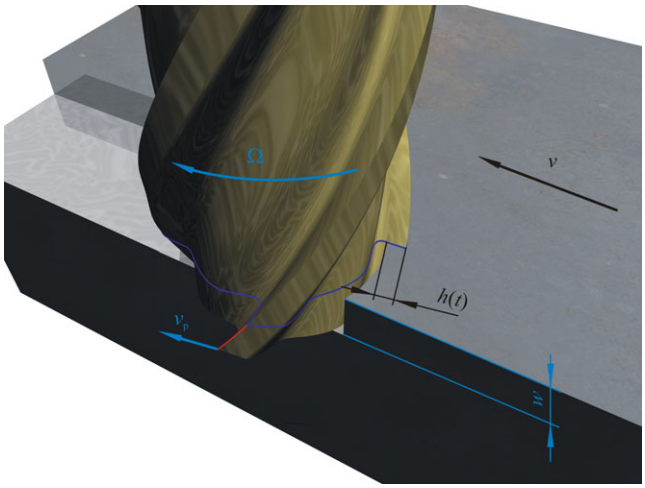

Figure 4: Parameters of the cutting force.

Models of the cutting force depends on numerous parameters. The most common used model is the so-called three-quarter role (figure 5. a). It is first used by Taylor for linear programming.

$$F_t = k\, h^{\frac{3}{4}}\, w v_p^{-0.1} = k_t\, h^{\frac{3}{4}}\, w \,, \tag{3}$$

where F_t – tangentional force

k, k_t – cutting coefficient, (technical parameters)

h – chip thickness

w – chip width

v_p – speed of cutting

In the milling process the peripheral speed (v_p) of the tool edge usually does not change. In that case v_p is absorbed into the parameter k_t.

The main problem with this function is that it has an infinite derivative at $h = 0$, which causes problems when the tool leaves or establish contact with the surface.

This function can be linearised around a working point (figure 5. b). This linearization also has a problem at $h = 0$, because it has a non-zero force at zero chip thickness. This problem can be fixed if we make a piecewise linear approximation to the cutting force so that it crosses the origin (figure 5. c).

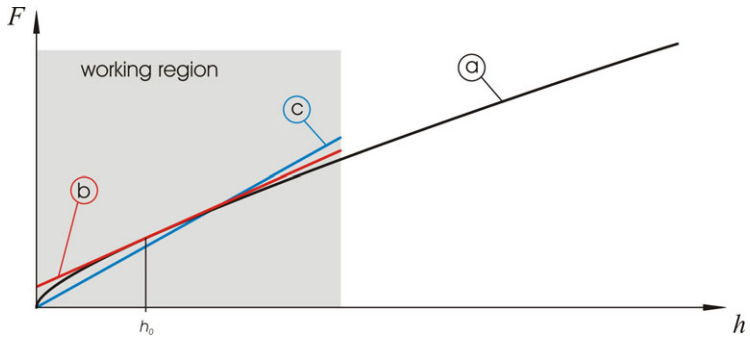

Figure 5: Linearization of the three-quarter role.

(a) three-quarter role, (b) tangent in h_0, (c) fitted line.

A polynomial function could also be used if we would like to study the non-linear behaviour of the system, or if we are close to $h = 0$. A quadratic polynomial function was used in [6] which was based on measurement.

In almost every case the tangential cutting force (F^t, shown in figure 8) is proportional to the radial cutting force (F^r, shown in figure 8) ([1, 2, 5, 7, 12]).

2.3. Cutting process

We now describe the models of the chip thickness. It usually contains of two parts. The first is the static chip thickness, which can be described by a rigid tool and rigid work-piece model. In this case the edge is moving on a trochoidal path (figure 6. a) relative to the surface. Such a description is used in [7].

We can approximate this motion with a series of circles (figure 6. b). This is a good approximation because the feed per tooth (f_z) is typically very small compared the diameter of the tool [7]. The feed per tool can calculated form the feed motion v, so

$$f_Z = \frac{2\pi v}{\Omega Z}. \tag{4}$$

In this case we can use a simple function for the chip thickness:

$$h_{stat} = f_Z \sin\left(\phi(t)\right), \tag{5}$$

where h_{stat} – static chip thickness

f_z – feed per tooth

$\phi(t)$ – angular position of the edge

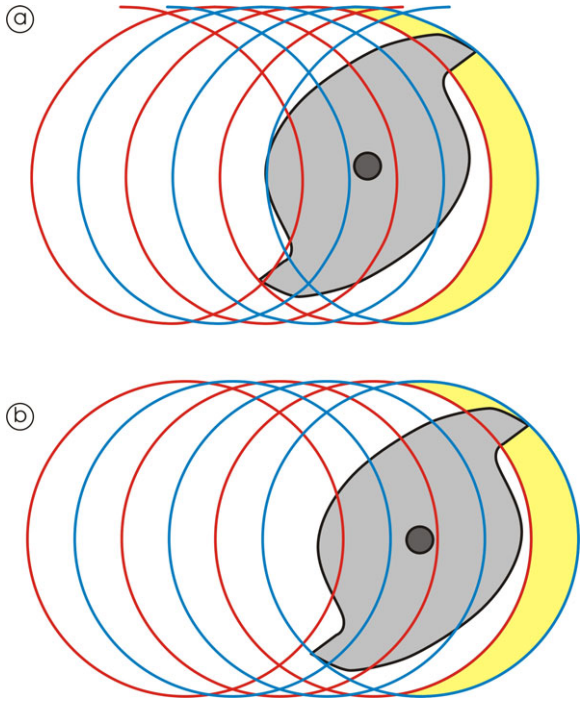

Figure 6: Trochoidal (a) and circular (b) path of the tool edge.

The second part of the chip thickness is the dynamic one. It arises from the vibration of the flexible system. The vibration also contains two parts. The first is generated by the periodic exciting force. This vibration has the same frequencies as the excitation force, and usually has small amplitude. In general case we assume that is small enough compared to the static chip thickness to neglect. In the case that it is larger we must use a much more complicated model for the static chip thickness. The second part of the vibration is a self-excited vibration caused by the time delay effect. It is due to the fact that the chip thickness depends on the edge path approximately one revolution of the tool ago.

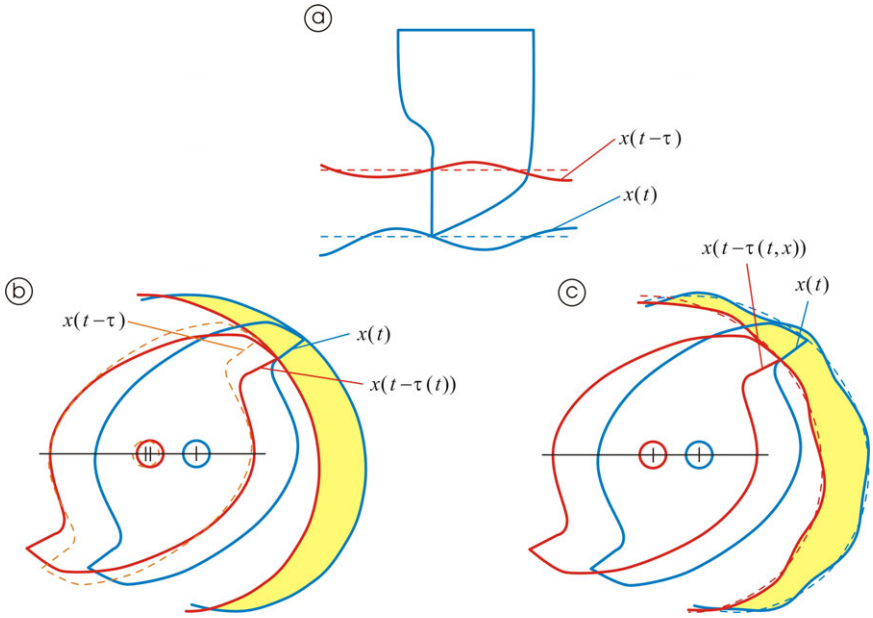

Figure 7: Constant (a), time dependent (b) and state dependent (c) delay.

It is very hard to make an analytical description of state dependent delay in the milling process, though some analytical solutions in the related problem of turning have been found [8]. Numerically, solutions can be calculated by time-domain simulation [5], though we shall use more sophisticated path-following methods.

Time dependent delay was considered in [7], but was shown that have a small effect on the stability.

The most commonly used model has a single constant delay. If we use a constant delay, self-excited vibrations die out in some regions of parameter space, and tend to large vibration elsewhere, thus it is not necessary to calculate surface profile solutions for this type of the vibration; only the stability calculation is needed. The boundary of this parameter region, where a bifurcation occurs, can be found by linear stability analysis. The non-linear terms only influence the type and the behaviour of the bifurcation.

The most important issue in calculating is to determine the surface prosperities at the permanent vibration of the stable system.

During milling, only the chatter-free process, where there is no self-excited vibration is acceptable, since in the case of chatter the surface has a poor quality and it overloads the machine-tool.

Chatter is caused by instability of the system, which occurs due to the time delay effect. Thus we have to calculate the stability of the system. Linear cutting force model which crosses the origin is suitable for finding the stability boundaries of the system, so we used this approximation of the cutting force.

Let us suppose that the vibration of the tool is small, so that we can use the simplest approximations of a static chip thickness (5) and a constant time delay in our model.

During our calculations, a 2 DoF, flexible tool/rigid work-piece model was used, both because the first modal frequency (in the x and y directions) are the most important due to the small damping, and also because it is the most commonly used model.

Surface calculations were made using both straight and helical edge tools.

3. Tool with straight edges

We begin by considering a simple model, of a tool with straight edges. Therefore we will be able to validate later, more complicate methods. In this case both analytical and numerical methods can be used, and their results can be compared with each other and with results in the literature.

3.1. System Equation

From the modal analysis we obtain the system equation:

$$\mathbf{M}\ddot{\mathbf{q}}(t)+\mathbf{K}\dot{\mathbf{q}}(t)+\mathbf{S}\mathbf{q}(t)=\mathbf{F}(t), \tag{6}$$

where $\mathbf{q}(t)$ and $\mathbf{F}(t)$ denote the displacement and cutting force vector in the $x-y$ plane. For a system with m vibration modes in x and y direction, the vectors $\mathbf{q}$ and $\mathbf{F}\in\mathbb{R}^{2m}$, and $\mathbf{M},\mathbf{K}$ and $\mathbf{S}\in\mathbb{R}^{2m\times 2m}$.

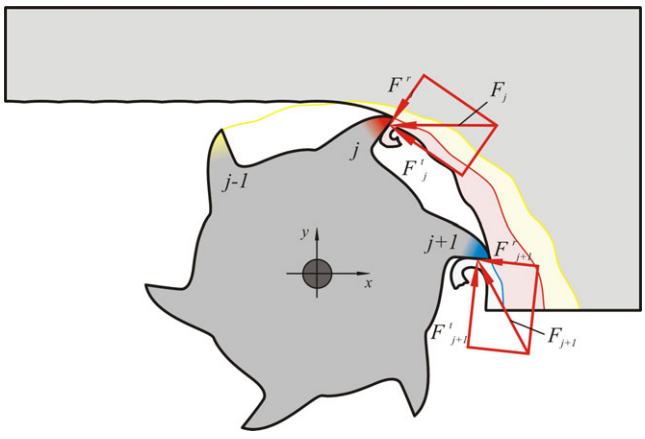

Figure 8: The tangent and radial components of the force in milling process.

The right hand side forcing function $\mathbf{F}$ originates from the cutting force. We can write it as a sum of the force from each individual tooth (see figure 8), so that

$$\mathbf{F}(t) = \sum_{j=0}^{Z-1} \mathbf{F}_j(t) = \sum_{j=0}^{Z-1} g_j\left(\phi_j(t)\right)\left(\mathbf{F}_j^{\mathrm{t}}(t) + \mathbf{F}_j^{\mathrm{r}}(t)\right), \tag{7}$$

where Z is the number of teeth, and ϕ_j is the angular position of the j^{th} tooth given by:

$$\phi_j(t) = t\Omega + j\frac{2\pi}{Z}, \tag{8}$$

and the step function g_j shows whether the j^{th} tooth is cutting or not, so

$$g_j\left(\phi_j(t)\right) = \begin{cases} 1, & \text{if } j^{\text{th}} \text{ tooth cutting} \\ 0, & \text{if } j^{\text{th}} \text{ tooth not cutting.} \end{cases} \tag{9}$$

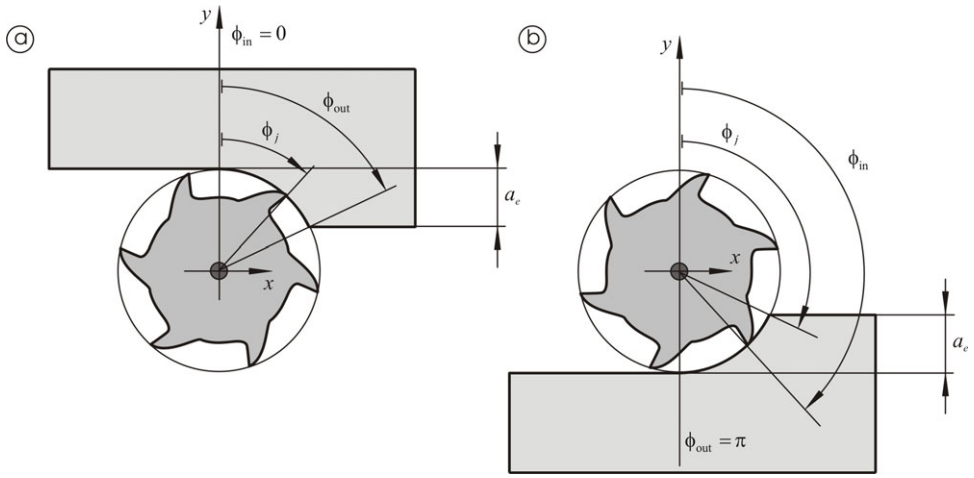

Figure 9: Step function (g_j) for up-milling (a) and down-milling (b).

Using the notation in figure 9, we can write g_j as

$$g_j\left(\phi_j(t)\right) = \begin{cases} 1, & \phi_{\text{in}} < \phi_j(t) < \phi_{\text{out}} \\ 0, & \text{otherwise.} \end{cases} \tag{10}$$

The parameters ϕ_{in} and ϕ_{out} are the angular position for which cutting begins and finishes respectively. If we assume that the vibration of the tool is small, then ϕ_{in} and ϕ_{out} are not state dependent. We consider two separate cases shown schematically in figure 9, known as up-milling and down-milling.

In the case of up-milling, ϕ_{in} and ϕ_{out} are defined by

$$\phi_{\text{in}} = 0 \text{ and } \quad \phi_{\text{out}} = \arccos\left(1 - 2\,a_{\text{ep}}\right), \tag{11}$$

and for down-milling by

$$\phi_{\text{in}} = \arccos\left(1 - 2(a_{\text{ep}} - 1)\right) \quad \text{and} \quad \phi_{\text{out}} = \pi\,, \tag{12}$$

where we define the parameter a_{ep} to be the dimensionless radial immersion relative to the diameter of the tool, D. For down-milling $a_{\text{ep}} \in [0,1]$ is given by

$$a_{\text{ep}} = \frac{a_{\text{e}}}{D}\,, \tag{13}$$

and for up-milling, $a_{\text{ep}} \in [1,2]$ is defined to be

$$a_{\text{ep}} = 2 - \frac{a_{\text{e}}}{D}\,, \tag{14}$$

where a_{e} is the radial immersion (shown in figure 9).

The angles ϕ_{in} and ϕ_{out} are shown graphically in figure 10.

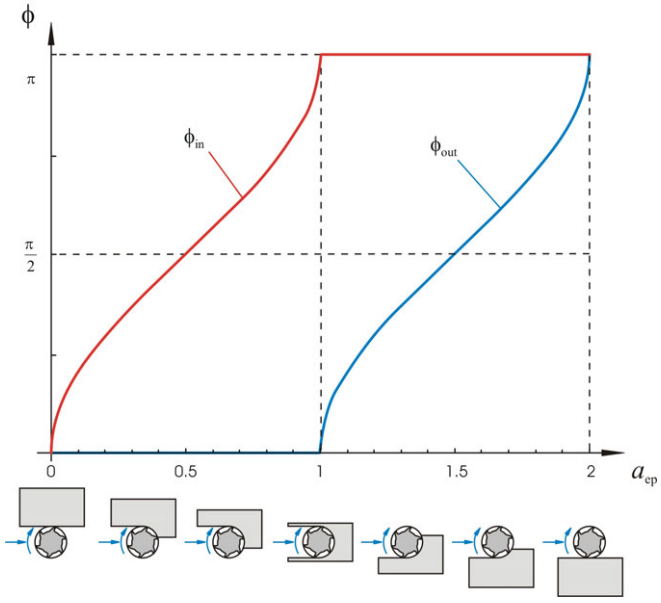

Figure 10: ϕ_{in} and ϕ_{out} as a function of a_{ep}.

We assume that the radial cutting force F_j^{r} is proportional to the tangential cutting force $F_j^{\text{t}}(t)$, so that:

$$\frac{F_j^{\text{t}}(t)}{F_j^{\text{r}}(t)} = \text{const} = k_{\text{r}}. \tag{15}$$

We can therefore write the cutting force $\mathbf{F}$ in x, y coordinates as

$$\mathbf{F}(t) = \sum_{j=0}^{Z-1} g_j\left(\phi_j(t)\right)\begin{bmatrix} -\cos\left(\phi_j(t)\right) - k_{\text{r}}\sin\left(\phi_j(t)\right) \\ \sin\left(\phi_j(t)\right) - k_{\text{r}}\cos\left(\phi_j(t)\right) \end{bmatrix} F_j^{\text{t}}(t). \tag{16}$$

We use a linear force model (described in section 2.2), so that

$$F_j^{\text{t}}(t) = w k_{\text{t}}\, h_j(t). \tag{17}$$

The chip thickness ($h_j(t)$) comprises two parts, the static and dynamic chip thicknesses. The static part is generated by the constant feed motion (v), while the fact that tool is non-rigid causes the dynamic part.

$$h_j(t) = h_j^{\text{stat}}(t) + h_j^{\text{din}}(t) \tag{18}$$

The static chip thickness can calculated (see section 2.3) as a projection of feed motion.

The feed per tooth, f_Z, is given by

$$f_Z = v\frac{2\pi}{\Omega Z}, \tag{19}$$

and hence, assuming a small tool vibration, we obtain

$$h_j^{\text{stat}}(t) = f_Z \sin\left(\phi_j(t)\right). \tag{20}$$

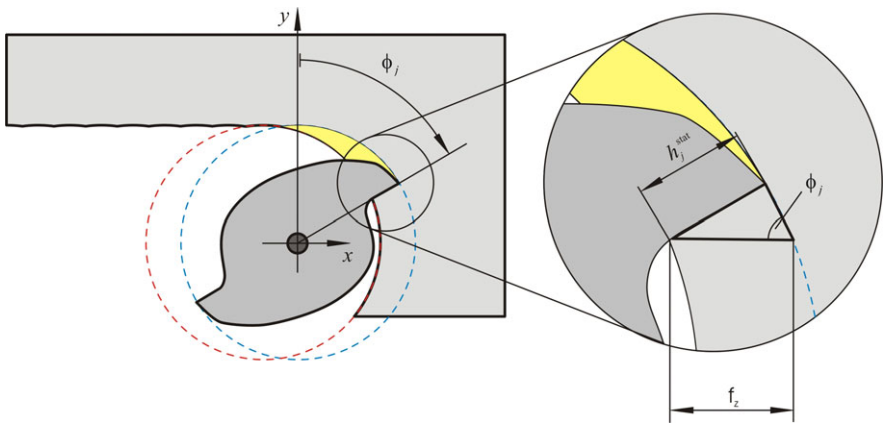

Figure 11: Projected static chip thickness $\left(h_j^{\text{stat}}\right)$.

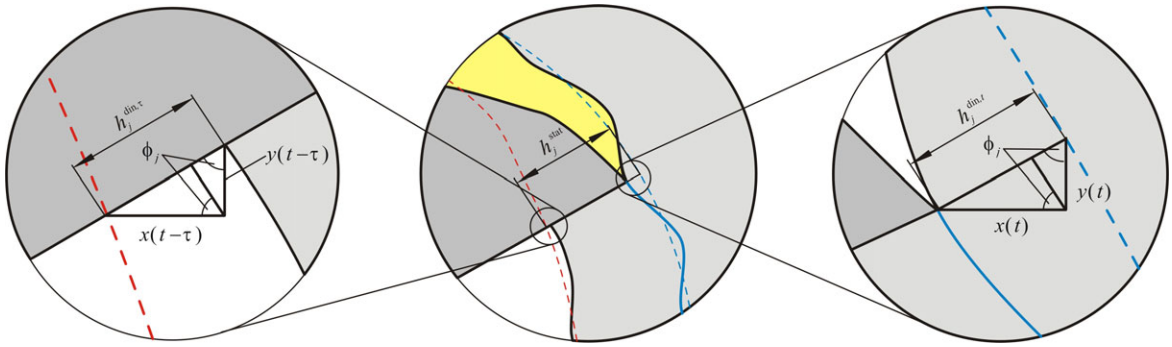

Figure 12: Dynamic part of the chip thickness $\left(h_j^{\mathrm{din}}\right)$.

The dynamic chip thickness is a function of the current and the previous tooth position.

$$h_j^{\mathrm{din}}(t) = h_j^{\mathrm{din,t}} - h_j^{\mathrm{din},\tau} = \left(x(t)-x(t-\tau)\right)\sin\left(\phi_j(t)\right)+\left(y(t)-y(t-\tau)\right)\cos\left(\phi_j(t)\right). \quad (21)$$

It is the dynamic chip thickness that causes the time delayed effect in the differential equation (6). The time delay is constant, generated by the tooth-passing frequency

$$\tau = \frac{2\pi}{\Omega Z}. \quad (22)$$

Substituting (21) and (20) into (18), we obtain

$$\begin{aligned} h_j(t) &= \left[\sin\left(\phi_j(t)\right) \quad \cos\left(\phi_j(t)\right)\right]\begin{bmatrix} f_Z + x(t)-x(t-\tau) \\ y(t)-y(t-\tau)\end{bmatrix} \\ &= \left[\sin\left(\phi_j(t)\right) \quad \cos\left(\phi_j(t)\right)\right]\left(\begin{bmatrix} f_Z \\ 0\end{bmatrix}+\mathbf{q}(t)-\mathbf{q}(t-\tau)\right), \end{aligned} \quad (23)$$

from which we can find the cutting force (16) , with the assumption of linearity (17)

$$\mathbf{F}(t) = \mathbf{W}(t)\left(\begin{bmatrix} f_Z \\ 0\end{bmatrix}+\mathbf{q}(t)-\mathbf{q}(t-\tau)\right). \quad (24)$$

The projection matrix $\mathbf{W}(t)$ is a periodic function, with period τ

$$\mathbf{W}(t)=\sum_{j=0}^{Z-1}\frac{wk_{\mathrm{t}}}{2}g_j(\phi_j(t))\,\mathbf{T}(\phi_j(t)), \tag{25}$$

where the transformation matrix is given by

$$\mathbf{T}(\phi_j(t))= \begin{bmatrix} -\sin(2\phi_j(t))-k_{\mathrm{r}}+k_{\mathrm{r}}\cos(2\phi_j(t)) & -1-\cos(2\phi_j(t))-k_{\mathrm{r}}\sin(2\phi_j(t)) \\ 1-\cos(2\phi_j(t))-k_{\mathrm{r}}\sin(2\phi_j(t)) & \sin(2\phi_j(t))-k_{\mathrm{r}}-k_{\mathrm{r}}\cos(2\phi_j(t)) \end{bmatrix}. \tag{26}$$

We note that the components of $\mathbf{W}(t)$ are exactly the same as in [1].

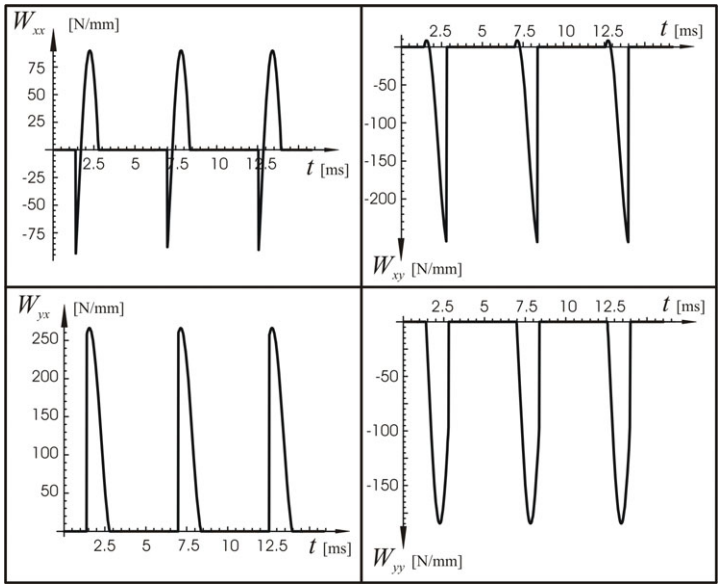

Figure 13: Component of W(t) as function of time for half immersion down-milling with a single fluted tooth. The parameters are $k_{\mathrm{t}}=644\cdot10^{6}\,[\mathrm{N/mm^2}]$, $k_{\mathrm{r}}=0.368$, $\Omega=20.5[\mathrm{krpm}]$.

We may now write the system equation (6) in the form:

$$\mathbf{M}\ddot{\mathbf{q}}(t)+\mathbf{K}\dot{\mathbf{q}}(t)+\left(\mathbf{S}-\mathbf{W}(t)\right)\mathbf{q}(t)=\mathbf{W}(t)\begin{bmatrix} f_z \\ 0 \end{bmatrix}-\mathbf{W}(t)\mathbf{q}(t-\tau)\,. \tag{27}$$

Equation (27) is linear, so we can separate it into two parts with new variables $\mathbf{x}$ and ξ

$$\mathbf{q}(t)=\mathbf{x}(t)+\xi(t)=\begin{bmatrix} x(t) \\ y(t) \end{bmatrix}+\begin{bmatrix} \xi(t) \\ \eta(t) \end{bmatrix}, \tag{28}$$

such that **x**(t) satisfies

$$\mathbf{M}\ddot{\mathbf{x}}(t)+\mathbf{K}\dot{\mathbf{x}}(t)+\mathbf{S}\mathbf{x}(t)=\mathbf{W}(t)\begin{bmatrix} f_z \\ 0 \end{bmatrix}=\mathbf{f}(t)\,. \tag{29}$$

Note that $\mathbf{f}(t)$ is periodic, with period τ. In this case $\mathbf{x}(t)$ also has the same period, so

$$\mathbf{x}(t)=\mathbf{x}(t-\tau)\,. \tag{30}$$

Equation (29) is the non-delayed part of the system equation. Substituting (28) into (27), and using (29) and (30), we obtain the delayed part of the system equation:

$$\mathbf{M}\ddot{\xi}(t)+\mathbf{K}\dot{\xi}(t)+\left(\mathbf{S}-\mathbf{W}(t)\right)\xi(t)=-\mathbf{W}(t)\xi(t-\tau) \tag{31}$$

Equation (31) is a system of second-order non-autonomous (parameter forced excited) linear delayed homogenous differential equations without external excitation. This part of the system equation describes the stability of the tool. It is essential to determine the stability of

the tool motion. If it is unstable, the tool vibration amplitude tends to infinity (and there is no need to calculate the surface).

If, on the other hand, the trivial solution of (31) ($\xi(t) = 0$) is stable, the motion of the tool centre is given by the solution of the non-delayed part of the system equation, (29). This is a system of second-order linear ordinary differential equations (ODE), with a non-smooth periodic excitation. This always has an asymptotically stable periodic solution because of the small damping. By using this solution we can compute the motion of the teeth, which generates the surface, neglecting transient motion.

3.2. Stability, time delay part

For equation (31) the constant zero is the only equilibrium, because it is linear DDE [19]. We must calculate the stability of this solution; there are several methods we can use.

The first method is time domain simulation. It is computationally expensive, partly because long integration times must be used; moreover the motion itself does not form part of the solution, and only stability information is important.

The second possible method is to use a Fourier series approximation of $\mathbf{W}(t)$. In case of the zeroth order approximation (ZOA) only the zeroth order Fourier term is used [4].

$$\mathbf{W} \cong \frac{1}{\tau}\int_0^{\tau} \mathbf{W}(t)dt \,. \tag{32}$$

With ZOA the characteristic polynomial can be used to calculate the stability boundaries. This approximation can be good at large radial immersion, but loses accuracy at small radial immersion.

The third possible approach is semi-discretization [3]. Detailed description of the method is written in section 3.2.1. The DDE (31) is approximated as a system of ordinary differential equations. In every ODE the time delayed terms and the excitation matrix are approached with constant values. The Floquet transition matrix over a period can be generated through the ODEs.

$$\boldsymbol{\xi}(t+\tau) = \boldsymbol{\Phi}\boldsymbol{\xi}(t) \,. \tag{33}$$

The system is stable if all eigenvalues of $\boldsymbol{\Phi}$ are smaller than 1 in modulus.

A fourth method is to use a package for Matlab, called DDE-BIFTOOL [10]. We can use this package for systems of delayed differential equations with several constant and state-dependent delays. It can calculate the stability of the steady-state solution and follow bifurcation curves in parameter space.

Because of the significant drawbacks of the first two methods, we use only methods 3 and 4.

3.2.1. Semi-discretization

The delayed part of the system equation (31) can be written as a system of first order delayed differential equations by using a new variable $\mathbf{u}$, where:

$$\mathbf{u}(t) = \begin{bmatrix} \dot{\xi}(t) \\ \dot{\eta}(t) \\ \xi(t) \\ \eta(t) \end{bmatrix} \tag{34}$$

$$\begin{aligned} \dot{\mathbf{u}}(t) &= \begin{bmatrix} -\mathbf{M}^{-1}\mathbf{K} & -\mathbf{M}^{-1}\left(\mathbf{S} - \mathbf{W}(t)\right) \\ \mathbf{I} & \mathbf{0} \end{bmatrix} \mathbf{u}(t) + \begin{bmatrix} \mathbf{0} & -\mathbf{M}^{-1}\mathbf{W}(t) \\ \mathbf{0} & \mathbf{0} \end{bmatrix} \mathbf{u}(t-\tau) \\ \dot{\mathbf{u}}(t) &= \mathbf{A}(t)\mathbf{u}(t) + \mathbf{B}(t)\mathbf{u}(t-\tau) \end{aligned} \tag{35}$$

We can approximate (35) with *m* coupled ODEs. The i^{th} ODE operates only for $t \in [t_i, t_i + \Delta t]$ where the length of the time interval Δt is given by

$$\Delta t = \frac{\tau}{m}. \tag{36}$$

In the i^{th} ODE we approximate $\mathbf{W}(t)$ and $\mathbf{u}(t-\tau)$ by:

$$\begin{aligned} \mathbf{u}(t-\tau) &= \frac{\mathbf{u}(t_{i-m}) + \mathbf{u}(t_{i-m+1})}{2} \\ \mathbf{W}(t) &\cong \mathbf{W}(t_i) = \mathbf{W}_i \qquad t \in [t_i, t_i + \Delta t] \end{aligned} \tag{37}$$

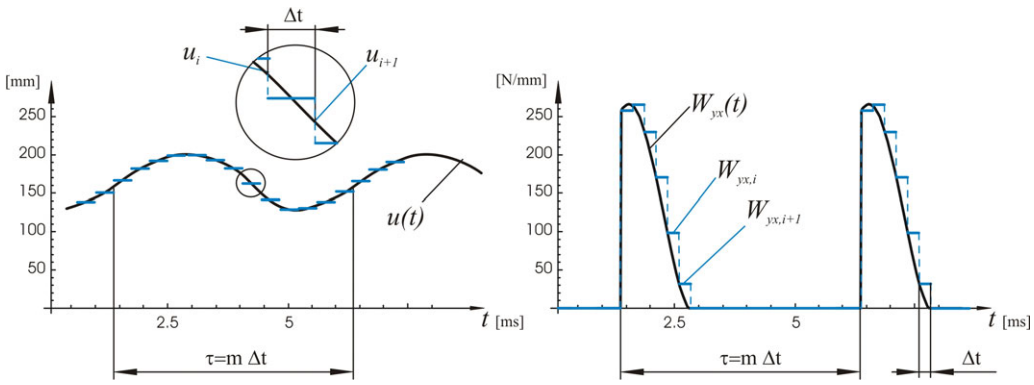

Figure 14: Approximation of $\mathbf{u}(t-\tau)$ and $\mathbf{W}(t)$.

We make the ODE approximation to (35) using (37), giving

$$\dot{\mathbf{u}}_i(t) = \mathbf{A}_i\mathbf{u}(t) + \mathbf{B}_i\frac{\mathbf{u}(t_{i-m}) + \mathbf{u}(t_{i-m+1})}{2} = \mathbf{A}_i\mathbf{u}(t) + \mathbf{v}_i \quad t \in [t_i, t_i + \Delta t] \tag{38}$$

The solution of (38) is:

$$\left.\begin{array}{l} \text{Particular}: \\ \dot{\mathbf{u}}_i(t) = 0 = \mathbf{A}_i\mathbf{u}_\mathrm{p} + \mathbf{v}_i \;\rightarrow = \mathbf{u}_\mathrm{p} = -\mathbf{A}_i^{-1}\mathbf{v}_i \\ \text{Homogeneous}: \\ \mathbf{u}_i(t) = \mathrm{e}^{\mathbf{A}_i(t-t_i)}\mathbf{c} \end{array}\right\} \mathbf{u}_i(t) = \mathrm{e}^{\mathbf{A}_i(t-t_i)}\mathbf{c} - \mathbf{A}_i^{-1}\mathbf{v}_i, \tag{39}$$

where the vector $\mathbf{c}$ is arbitrary. We determine it using the initial condition

$$\mathbf{u}(t_i) = \mathbf{u}_i \tag{40}$$

so

$$\mathbf{u}_i(t_i) = \mathrm{e}^{\mathbf{A}_i(t_i-t_i)}\mathbf{c} - \mathbf{A}_i^{-1}\mathbf{v}_i = \mathbf{u}_i \;\; \mathbf{c} = \mathbf{u}_i + \mathbf{A}_i^{-1}\mathbf{v}. \tag{41}$$

Thus the solution for the $t \in [t_i, t_i + \Delta t]$ is

$$\mathbf{u}_i(t) = \mathrm{e}^{\mathbf{A}_i(t-t_i)}(\mathbf{u}_i + \mathbf{A}_i^{-1}\mathbf{v}) - \mathbf{A}_i^{-1}\mathbf{v}_i, \tag{42}$$

and hence, at the end of time interval

$$\mathbf{u}_i(t_i + \Delta t) = \mathbf{u}_i(t_{i+1}) = \mathbf{u}_{i+1} = \mathrm{e}^{\mathbf{A}_i\Delta t}(\mathbf{u}_i + \mathbf{A}_i^{-1}\mathbf{v}) - \mathbf{A}_i^{-1}\mathbf{v}_i \tag{43}$$

This can be simplified using (38) to give

$$\mathbf{u}_{i+1} = \mathbf{P}_i\mathbf{u}_i + \mathbf{R}_i\big(\mathbf{u}(t_{i-m}) + \mathbf{u}(t_{i-m+1})\big), \tag{44}$$

where

$$\mathbf{P}_i = \mathrm{e}^{\mathbf{A}_i\Delta t} \qquad \text{and} \qquad \mathbf{R}_i = \frac{(\mathrm{e}^{\mathbf{A}_i\Delta t} - \mathbf{I})\mathbf{A}_i^{-1}\mathbf{B}_i}{2}. \tag{45}$$

Using a new variable $\mathbf{v}_i$, we can define a discrete map

$$\mathbf{v}_i = \begin{bmatrix} \mathbf{u}_i \\ \mathbf{u}_{i-1} \\ \vdots \\ \mathbf{u}_{i-m} \end{bmatrix} \qquad \rightarrow \qquad \mathbf{v}_{i+1} = \mathbf{Z}_i\mathbf{v}_i, \tag{46}$$

with coefficient matrix $\mathbf{Z}_i \in \mathbb{R}^{(4(m+1)\times 4(m+1))}$ given by

$$\mathbf{Z}_i = \begin{bmatrix} \mathbf{P}_i & \mathbf{0} & \cdots & \mathbf{0} & \mathbf{R}_i & \mathbf{R}_i \\ \mathbf{I} & \mathbf{0} & \cdots & \mathbf{0} & \mathbf{0} & \mathbf{0} \\ \mathbf{0} & \mathbf{I} & \cdots & \mathbf{0} & \mathbf{0} & \mathbf{0} \\ \vdots & \vdots & \ddots & \vdots & \vdots & \vdots \\ \mathbf{0} & \mathbf{0} & \cdots & \mathbf{I} & \mathbf{0} & \mathbf{0} \\ \mathbf{0} & \mathbf{0} & \cdots & \mathbf{0} & \mathbf{I} & \mathbf{0} \end{bmatrix}. \tag{47}$$

We can reduce the size of these matrices. Some elements of $\mathbf{v}_i$ can be omitted out because $\mathbf{R}_i$ only has elements in the upper right side, due to the fact that (31) is not neutral. Hence we may write a new variable $\widetilde{\mathbf{v}}_i$ such that

$$\widetilde{\mathbf{v}}_i = \begin{bmatrix} \dot{\xi}_i & \dot{\eta}_i & \xi_i & \eta_i & \xi_{i-1} & \eta_{i-1} & \cdots & \xi_{i-m} & \eta_{i-m} \end{bmatrix}^T \tag{48}$$

and the new coefficient matrix $\widetilde{\mathbf{Z}}_i \in \mathbb{R}^{(2(m+2)\times 2(m+2))}$ such that

$$\widetilde{\mathbf{Z}}_i = \begin{bmatrix} P_{11,i} & P_{12,i} & P_{13,i} & P_{14,i} & 0 & \cdots & 0 & R_{13,i} & R_{14,i} & R_{13,i} & R_{14,i} \\ P_{21,i} & P_{22,i} & P_{23,i} & P_{24,i} & 0 & \cdots & 0 & R_{23,i} & R_{24,i} & R_{23,i} & R_{24,i} \\ P_{31,i} & P_{32,i} & P_{33,i} & P_{34,i} & 0 & \cdots & 0 & R_{33,i} & R_{34,i} & R_{33,i} & R_{34,i} \\ P_{41,i} & P_{42,i} & P_{43,i} & P_{44,i} & 0 & \cdots & 0 & R_{43,i} & R_{44,i} & R_{43,i} & R_{44,i} \\ 0 & 0 & 1 & 0 & 0 & \cdots & 0 & 0 & 0 & 0 & 0 \\ 0 & 0 & 0 & 1 & 0 & \cdots & 0 & 0 & 0 & 0 & 0 \\ 0 & 0 & 0 & 0 & 1 & \cdots & 0 & 0 & 0 & 0 & 0 \\ \vdots & \vdots & \vdots & \vdots & \vdots & \ddots & \vdots & \vdots & \vdots & \vdots & \vdots \\ 0 & 0 & 0 & 0 & 0 & \cdots & 1 & 0 & 0 & 0 & 0 \\ 0 & 0 & 0 & 0 & 0 & \cdots & 0 & 1 & 0 & 0 & 0 \\ 0 & 0 & 0 & 0 & 0 & \cdots & 0 & 0 & 1 & 0 & 0 \end{bmatrix} \tag{49}$$

The Floquet transition matrix over a period can be generated as a product of $\widetilde{\mathbf{Z}}_i$ matrices

$$\mathbf{\Phi} = \widetilde{\mathbf{Z}}_{m-1}\widetilde{\mathbf{Z}}_{m-2}\ldots\widetilde{\mathbf{Z}}_2\widetilde{\mathbf{Z}}_1\widetilde{\mathbf{Z}}_0 . \tag{50}$$

The stability of the non-delayed part of the system equation is determined by the eigenvalues of $\mathbf{\Phi}$. If all the eigenvalues are located in the unit circle in the complex plane then the zero solution of is (31) stable.

The zero solution can lose its stability in two ways. The first called a Hopf bifurcation is when two complex conjugate eigenvalues cross the unit circle [2]. In this case the time period of the vibration is different from the time delay. In a real milling process this phenomenon causes chatter characterized by quasi-periodic vibration.

The second way is when an eigenvalue crosses the unit circle at the point -1. This bifurcation is called a flip or periodic doubling bifurcation, because the time period of the vibration is twice as long as the time delay, which causes chatter characterized by periodic vibration.

In our linear system both above mentioned vibrations tend to infinity if the system is unstable.

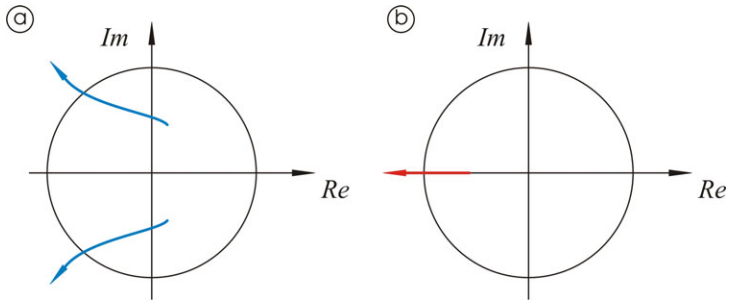

Figure 15: Stability losing by Hopf (a) and flip (b) bifurcation.

A stability chart can be made by calculating the stability in a grid in parameter space. In our system (31) the Hopf bifurcation lines have a lobe structure, with flip bifurcation lenses (see figure 16), exactly as in [2].

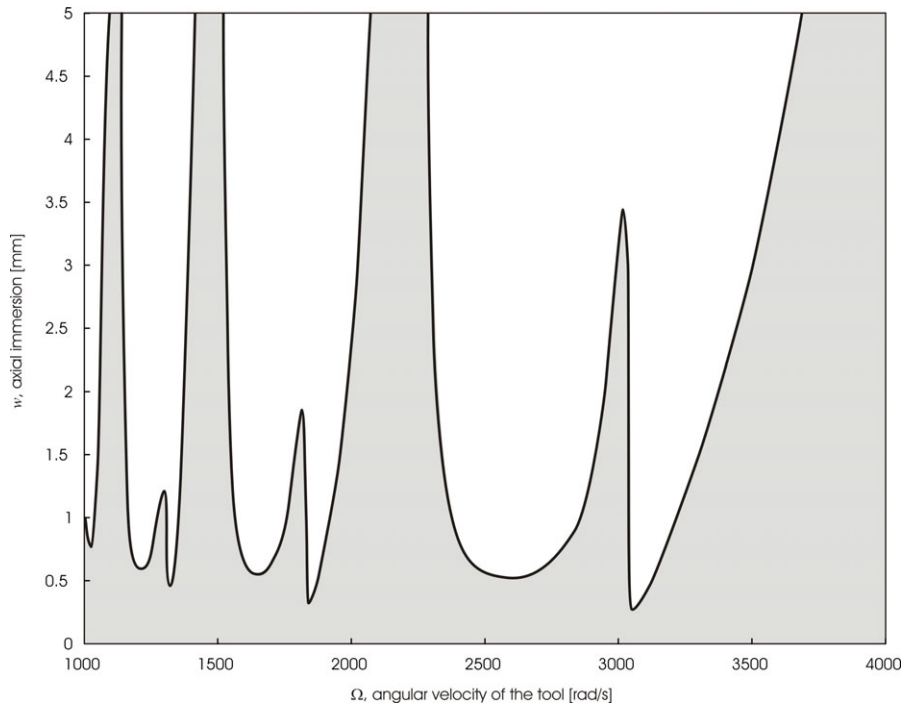

Figure 16: Stability chart of the system computed by semi-discretization method. Parameters are $Z = 1$, $a_{ep} = 0.05$.

Producing a chart with acceptable quality takes a very long time. A chart with acceptable quality and precision calculated more than 2 hour by using Matlab in Windows. It is not necessary to compute the stability at every point on the grid, because only the stability boundaries are needed. If we calculate the stability around the boundaries, we can reduce the calculation time by a factor of about 10. For this reason the chart was initially computed on a coarse mesh. Those segments, where the stability changed were divided to four parts and recomputed. This process was repeated until the diagram was of prescribed quality.

3.2.2. DDE-BIFTOOL

To validate the semi-discretization method the Matlab package, called DDE-BIFTOOL was used. This program is made for autonomous systems of DDEs. We modified the program to be able to compute a parametrically-excited system. Hence the constant zero solution of (31) can be described as a periodic solution. This is needed to permit consideration of a periodic excitation. The boundaries of regions stability of the zero solution were followed in the parameter space by a predictor-corrector method.

We check the semi-discretization method, and the stability lines of DDE-BIFTOOL fit very well into the stability boundaries of the semi-discretization, as shown in figure 17.

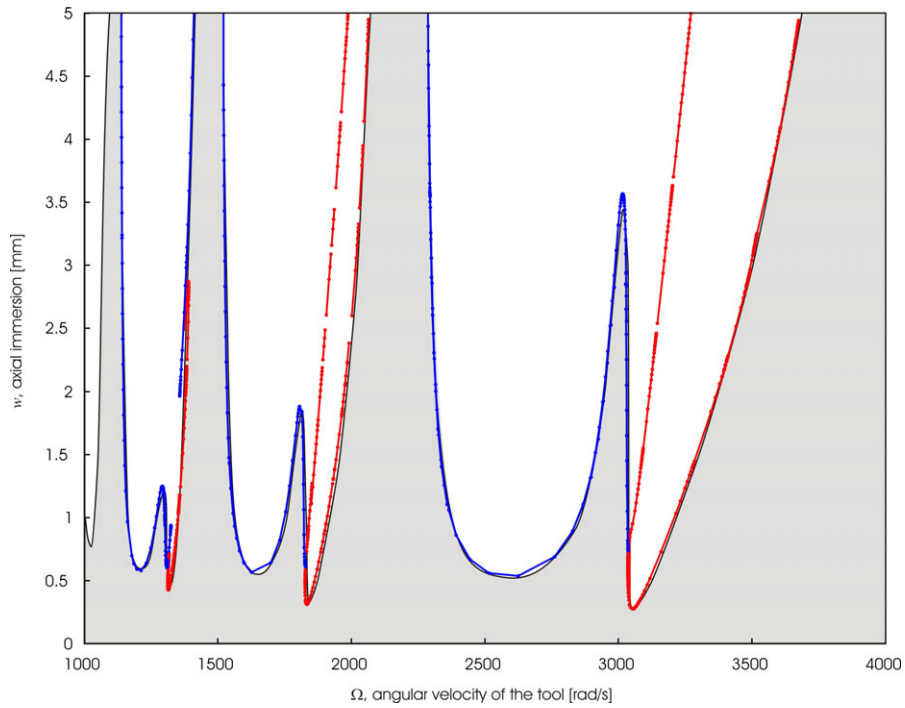

Figure 17: Stability chart of the system using DDE-BIFTOOL.

Parameters are $Z = 1$, $a_{ep} = 0.05$.

3.2.3. Transient

In the case that the zero solution is stable, then the transient solution dies out. The amplitude of the transient decreases according to μ_1, which is the modulus of the biggest eigenvalue of $\mathbf{\Phi}$. Over a period

$$\frac{\left|\mathbf{u}_{\text{transient}}(t+\tau)\right|}{\left|\mathbf{u}_{\text{transient}}(t)\right|} \cong \left|\mu_1\right| \tag{51}$$

Near to the stability boundary, μ_1 is very close to 1, so the transient takes a very long time to die out.

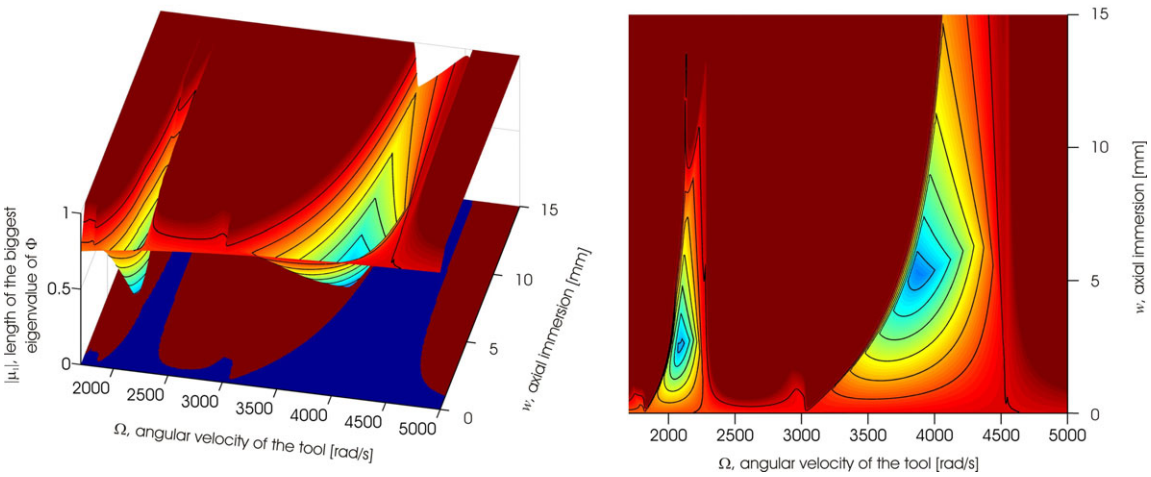

Figure 18: Modulus of the biggest eigenvalue of $\mathbf{\Phi}$ over the stability chart.

Parameters are $Z = 1$, $a_{\text{ep}} = 0.1$.

Figure 18 shows that the modulus of μ_1 decreases at smaller angular velocity. There are areas on the stability chart where the transient dies out much faster.

3.3. Surface, non-delay part

If we use a rigid tool and rigid work-piece model, the surface roughness (μ_0) which is the biggest deflection of the surface can be calculated in a simple way by approaching the tooth path as a circle, so

$$\mu_0 = R\left(1-\sqrt{1-\left(\frac{f_z}{2R}\right)}\right) \cong \frac{f_z^{\,2}}{8\mathrm{R}}, \tag{52}$$

where R is the radius of the tool.

If the delayed part of (31) has a stable zero solution, then the motion of the tool centre is described only by the solution of the non-delayed part, (29). We now describe the computation of the surface, during which we assume that transient motion can be neglected.

The only difficulty occurs because the function $\mathbf{f}(t)$ is non-smooth. There are different ways to solve this problem and get the particular solution of the equation (29).

The first is to use the first N_F terms of the Fourier series of $\mathbf{f}(t)$ instead of $\mathbf{f}(t)$ itself. Good approximation can usually be achieved by using the first 10 terms of the series ($N_F = 10$) according to [1]

$$\mathbf{f}(t) \cong \mathbf{a}_0 + \sum_{l=1}^{N_F} \mathbf{a}_l \cos\left(\frac{2\pi l t}{\tau}\right) + \mathbf{b}_l \sin\left(\frac{2\pi l t}{\tau}\right). \tag{53}$$

In this case the solution can be given as a similar trigonometric function

$$\mathbf{x}(t) \cong \mathbf{c}_0 + \sum_{l=1}^{N_F} \mathbf{c}_l \cos\left(\frac{2\pi l t}{\tau}\right) + \mathbf{d}_l \sin\left(\frac{2\pi l t}{\tau}\right). \tag{54}$$

By using (53) and (54), equation (29) can be separated to find the constants $\mathbf{c}_l$ and $\mathbf{d}_l$ by matching the coefficients of sin and cos.

$$\begin{bmatrix}\mathbf{c}_l\\ \mathbf{d}_l\end{bmatrix}=\begin{bmatrix}\mathbf{S}-\left(\frac{2\pi l}{\tau}\right)^2\mathbf{M} & \mathbf{K}\left(\frac{2\pi l}{\tau}\right)\\ -\mathbf{K}\left(\frac{2\pi l}{\tau}\right) & \mathbf{S}-\left(\frac{2\pi l}{\tau}\right)^2\mathbf{M}\end{bmatrix}^{-1}\begin{bmatrix}\mathbf{a}_l\\ \mathbf{b}_l\end{bmatrix} \qquad l=1,2,\ldots,N_{\mathrm{F}}. \qquad (55)$$

The second possible solution method gives an analytical solution of (29). We observe that $\mathbf{f}(t)$ is non-smooth only at the points where the $g_j(\phi_j(t))$ functions switch. Equation (29) can be solved analytically between these switching points.

A third possible method is time domain simulation. This kind of method always can be easily used. Its biggest drawback is that the transient motion cannot be neglected, and so the simulation time must be enough long to let it die out. The size of the surface quality is of the order of micrometers, so the error due to the transient motion must be significantly smaller than that value. The relative damping factor of the machine-tools is very small, however, around 0.01, so the size of the transient is halved about every 11^{th} period; too long for practical use.

3.3.1. Analytical method

The quality of the surface is important principally in the surface finishing process. In this process the radial immersion is always small and the tool has just a few teeth, which means that usually just one tooth is cutting. This approximation is valid if

$$Z \le \frac{2\pi}{\phi_{\text{out}}-\phi_{\text{in}}}. \qquad (56)$$

For example, where the radial immersion is 0.25, the maximal number of teeth is 6. In this case the solution of (29) can be solved in two parts (cutting and flying), and patched together to ensure continuity of the solution.

The particular solution is periodic and has the same time period as the excitation, τ , so that

$$\begin{aligned} \mathbf{x}(t) &= \mathbf{x}(t+\tau), \\ \dot{\mathbf{x}}(t) &= \dot{\mathbf{x}}(t+\tau). \end{aligned} \tag{57}$$

If equation (29) is solved with a general initial starting point, and satisfies (57) then it is a periodic solution. The initial values can be found more easily by using a new time coordinate, relative to the beginning of the cutting phase.

$$\begin{aligned} \tilde{t} &= t - T_{\text{in}} = t - \frac{\phi_{\text{in}}}{\Omega} \\ \phi(\tilde{t}) &= \tilde{t}\,\Omega + \phi_{\text{in}}\,. \end{aligned} \tag{58}$$

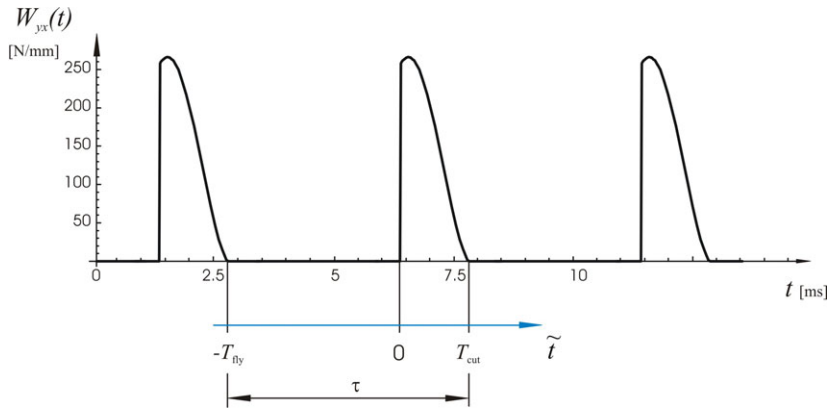

Figure 19: New time coordinate for the periodic solution.

Eq. (29) can be written in first order form:

$$\mathbf{u}(\tilde{t}) = \left[\dot{x}(\tilde{t}) \quad \dot{y}(\tilde{t}) \quad x(\tilde{t}) \quad y(\tilde{t})\right]^T, \tag{59}$$

$$\dot{\mathbf{u}}(\tilde{t}) = \mathbf{A}\mathbf{u}(\tilde{t}) + \begin{bmatrix} \mathbf{M}^{-1}\mathbf{f}(\tilde{t}) \\ \mathbf{0} \end{bmatrix}, \tag{60}$$

where

$$\mathbf{A} = \begin{bmatrix} -\mathbf{M}^{-1}\mathbf{K} & -\mathbf{M}^{-1}\mathbf{S} \\ \mathbf{I} & \mathbf{0} \end{bmatrix}, \tag{61}$$

and separated into the two phases: first flying motion

$$\begin{aligned} &\dot{\mathbf{u}}_{\text{fly}}(\tilde{t}) = \begin{bmatrix} -\mathbf{M}^{-1}\mathbf{K} & -\mathbf{M}^{-1}\mathbf{S} \\ \mathbf{I} & \mathbf{0} \end{bmatrix} \mathbf{u}_{\text{fly}}(\tilde{t}) \\ &\dot{\mathbf{u}}_{\text{fly}}(\tilde{t}) = \mathbf{A}\mathbf{u}_{\text{fly}}(\tilde{t}) \qquad\qquad \tilde{t} \in [-T_{\text{fly}}, 0] \end{aligned} \tag{62}$$

and second, cutting motion:

$$\dot{\mathbf{u}}_{\text{cut}}(\tilde{t}) = \mathbf{A}\mathbf{u}_{\text{cut}}(\tilde{t}) + \begin{bmatrix} \mathbf{M}^{-1}\mathbf{f}(\tilde{t}) \\ \mathbf{0} \end{bmatrix} \qquad \tilde{t} \in [0, T_{\text{cut}}], \tag{63}$$

where

$$T_{\text{fly}} = \frac{\phi_{\text{out}} - \phi_{\text{in}}}{\Omega}; \qquad T_{\text{cut}} = \tau - T_{\text{fly}}. \tag{64}$$

Excitation of (63) can be written in a trigonometrical form:

$$\begin{aligned} &\mathbf{M}^{-1}\,\mathbf{f}(\tilde{t}) = \mathbf{M}^{-1}\left(\mathbf{a}_{\text{k}} + \mathbf{a}_{\text{s}}\sin\left(2\phi(\tilde{t})\right) + \mathbf{a}_{\text{c}}\cos\left(2\phi(\tilde{t})\right)\right) \\ &= \mathbf{M}^{-1}\left(\mathbf{v}_{\text{k}} + \mathbf{v}_{\text{s}}\sin\left(2\Omega\tilde{t}\right) + \mathbf{v}_{\text{c}}\cos\left(2\Omega\tilde{t}\right)\right) \end{aligned}, \tag{65}$$

where

$$\mathbf{v}_{\mathrm{k}} = \frac{f_Z\, w k_{\mathrm{t}}}{2}\begin{bmatrix} -k_{\mathrm{r}} \\ 1 \end{bmatrix}; \quad \mathbf{v}_{\mathrm{s}} = \frac{f_Z\, w k_{\mathrm{t}}}{2}\begin{bmatrix} -\cos(2\phi_{\mathrm{in}}) - k_{\mathrm{r}}\sin(2\phi_{\mathrm{in}}) \\ -k_{\mathrm{r}}\cos(2\phi_{\mathrm{in}}) + \sin(2\phi_{\mathrm{in}}) \end{bmatrix};$$
$$\mathbf{v}_{\mathrm{c}} = \frac{f_Z\, w k_{\mathrm{t}}}{2}\begin{bmatrix} k_{\mathrm{r}}\cos(2\phi_{\mathrm{in}}) - \sin(2\phi_{\mathrm{in}}) \\ -\cos(2\phi_{\mathrm{in}}) - k_{\mathrm{r}}\sin(2\phi_{\mathrm{in}}) \end{bmatrix}. \tag{66}$$

Let the initial values be

$$\mathbf{u}(0) = \mathbf{u}_0 = \begin{bmatrix} \mathbf{v}_0 & \mathbf{x}_0 \end{bmatrix}^T = \begin{bmatrix} \dot{x}_0 & \dot{y}_0 & x_0 & y_0 \end{bmatrix}^T, \tag{67}$$

Then the solution of (60) is:

$$\left.\begin{aligned} \mathbf{u}_{\mathrm{fly}}(\tilde{t}) &= \mathrm{e}^{\mathbf{A}\tilde{t}}\mathbf{c} \\ \mathbf{u}_{\mathrm{fly}}(0) &= \mathbf{c} = \mathbf{u}_0 \end{aligned}\right\} \mathbf{u}_{\mathrm{fly}}(\tilde{t}) = \mathrm{e}^{\mathbf{A}\tilde{t}}\mathbf{u}_0 \qquad \tilde{t} \in [-T_{\mathrm{fly}}, 0]. \tag{68}$$

The particular solution of the cutting motion equation (63) also has the same trigonometrical form as $\mathbf{f}(\tilde{t})$:

$$\mathbf{u}_{\mathrm{p,cut}}(\tilde{t}) = \mathbf{m} + \mathbf{l}\sin(2\Omega\tilde{t}) + \mathbf{k}\cos(2\Omega\tilde{t}). \tag{69}$$

$$\dot{\mathbf{u}}_{\mathrm{p,cut}}(\tilde{t}) = 2\Omega\mathbf{l}\cos(2\Omega\tilde{t}) - 2\Omega\mathbf{k}\sin(2\Omega\tilde{t}) \tag{70}$$

The coefficients **m**, **l**, **k** can be calculated using Eq. (63), again separated according to the trigonometrical functions:

$$\begin{bmatrix} 1 \\ \sin(2\Omega\tilde{t}) \\ \cos(2\Omega\tilde{t}) \end{bmatrix}^T \begin{bmatrix} -\mathbf{A} & \mathbf{0} & \mathbf{0} \\ \mathbf{0} & -\mathbf{A} & -2\Omega\mathbf{I} \\ \mathbf{0} & 2\Omega\mathbf{I} & -\mathbf{A} \end{bmatrix} \begin{bmatrix} \mathbf{m} \\ \mathbf{l} \\ \mathbf{k} \end{bmatrix} = \begin{bmatrix} 1 \\ \sin(2\Omega\tilde{t}) \\ \cos(2\Omega\tilde{t}) \end{bmatrix}^T \begin{bmatrix} \mathbf{M}^{-1}\mathbf{v}_k \\ \mathbf{0} \\ \mathbf{M}^{-1}\mathbf{v}_s \\ \mathbf{0} \\ \mathbf{M}^{-1}\mathbf{v}_c \\ \mathbf{0} \end{bmatrix} \tag{71}$$

$$\begin{bmatrix} \mathbf{m} \\ \mathbf{l} \\ \mathbf{k} \end{bmatrix} = \begin{bmatrix} -\mathbf{A} & \mathbf{0} & \mathbf{0} \\ \mathbf{0} & -\mathbf{A} & -2\Omega\mathbf{I} \\ \mathbf{0} & 2\Omega\mathbf{I} & -\mathbf{A} \end{bmatrix}^{-1} \begin{bmatrix} \mathbf{M}^{-1}\mathbf{v}_k \\ \mathbf{0} \\ \mathbf{M}^{-1}\mathbf{v}_s \\ \mathbf{0} \\ \mathbf{M}^{-1}\mathbf{v}_c \\ \mathbf{0} \end{bmatrix}. \tag{72}$$

Hence the homogenous part of equation (63) is

$$\mathbf{u}_{\mathrm{h,cut}}(\tilde{t}) = \mathrm{e}^{\mathbf{A}\tilde{t}}\mathbf{c}\,. \tag{73}$$

The **c** vector can be found by using the initial values:

$$\begin{aligned} &\mathbf{u}_{\mathrm{cut}}(\tilde{t}) = \mathbf{u}_{\mathrm{h,cut}}(\tilde{t}) + \mathbf{u}_{\mathrm{p,cut}}(\tilde{t}) = \mathrm{e}^{\mathbf{A}\tilde{t}}\mathbf{c} + \mathbf{m} + \mathbf{l}\sin(2\Omega\tilde{t}) + \mathbf{k}\cos(2\Omega\tilde{t}) \\ &\mathbf{u}_{\mathrm{cut}}(\tilde{t}=0) = \mathbf{u}_0 = \mathbf{c} + \mathbf{m} + \mathbf{k} = \mathbf{u}_0 \\ &\mathbf{c} = \mathbf{u}_0 - \mathbf{m} - \mathbf{k} \qquad\qquad \tilde{t} \in [0, T_{\mathrm{cut}}]. \end{aligned} \tag{74}$$

The solution of cutting motion is

$$\mathbf{u}_{\mathrm{cut}}(\tilde{t}) = \mathbf{u}_{\mathrm{h,cut}}(\tilde{t}) + \mathbf{u}_{\mathrm{p,cut}}(\tilde{t}) = \mathrm{e}^{\mathbf{A}\tilde{t}}(\mathbf{u}_0 - \mathbf{m} - \mathbf{k}) + \mathbf{m} + \mathbf{l}\sin(2\Omega\tilde{t}) + \mathbf{k}\cos(2\Omega\tilde{t}). \tag{75}$$

The particular solution satisfies (57), so that

$$\begin{aligned}
&\mathbf{u}(-T_{\text{fly}}) = \mathbf{u}(-T_{\text{fly}} + \tau) = \mathbf{u}(T_{\text{cut}}),\\
&\mathbf{u}_{\text{fly}}(-T_{\text{fly}}) = \mathbf{u}_{\text{cut}}(T_{\text{cut}}),\\
&\mathrm{e}^{\mathbf{A}(-T_{\text{fly}})}\mathbf{u}_0 = \mathrm{e}^{\mathbf{A}T_{\text{cut}}}(\mathbf{u}_0 - \mathbf{m} - \mathbf{k}) + \mathbf{m} + \mathbf{l}\sin(2\Omega T_{\text{cut}}) + \mathbf{k}\cos(2\Omega T_{\text{cut}}),\\
&\mathbf{u}_0 = \left(\mathrm{e}^{\mathbf{A}(-T_{\text{fly}})} - \mathrm{e}^{\mathbf{A}T_{\text{cut}}}\right)^{-1}\left(\left(\mathbf{I} - \mathrm{e}^{\mathbf{A}T_{\text{cut}}}\right)\mathbf{m} + \left(\mathbf{I}\cos(2\Omega T_{\text{cut}}) - \mathrm{e}^{\mathbf{A}T_{\text{cut}}}\right)\mathbf{k} + \mathbf{I}\,\mathbf{l}\sin(2\Omega T_{\text{cut}})\right).
\end{aligned} \tag{76}$$

Thus the motion of the tool centre can be calculated analytically. In order to generate the surface we have to calculate the motion of the tooth edges. The vibration of the teeth is just the same as the tool centre, but the vibration superposes on a circle with the radius (R) of the tool. Every point of the tool edge has the same path in its own relative time frame. The motions of the edges are given by

$$\mathbf{e}(\tilde{t}) = \mathbf{e}_j(\tilde{t}) = \begin{bmatrix} x(\tilde{t}) \\ y(\tilde{t}) \end{bmatrix} + \begin{bmatrix} R\cos(\phi_j(\tilde{t})) \\ R\sin(\phi_j(\tilde{t})) \end{bmatrix}. \tag{77}$$

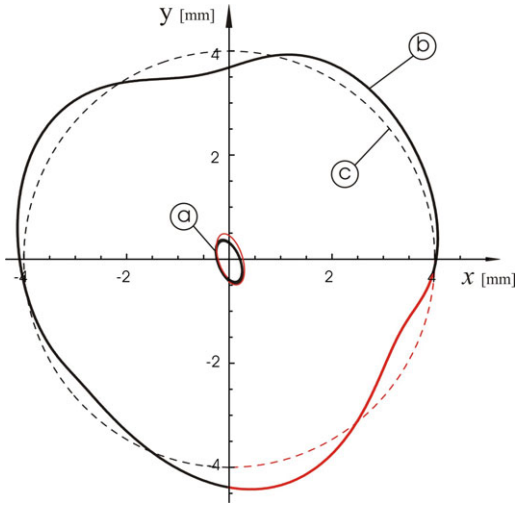

Figure 20: Motion of the tool centre (a) and tooth edge path of flexible (b) and rigid (c) tool. Red lines denote the cutting phase, black lines denote the flying phase.
Parameters are $Z = 1$, $\Omega = 1125[rad/s]$, $w = 0.4[mm]$, $f_z = 0.15[mm]$, $a_{\text{ep}} = 1.5$.

3.3.2. Time domain simulation

The time domain simulation is made by the simplest Euler method. The time step (Δt) of the simulation was changed to consider its effect on the simulation. We observed that if

$$\Delta t \le \frac{\tau}{1000}, \tag{78}$$

there was no significant change in the edge path. On a simulated edge path, shown in figure 21, we can see the problem of the small damping. We cannot even use the edge path if we simulate over a hundred periods, because the transient motion is still large relative to the surface quality. In spite of this fact the shape of the vibration is acceptable to validate the analytical solution. The difference between the two different methods is shown in figure 22.

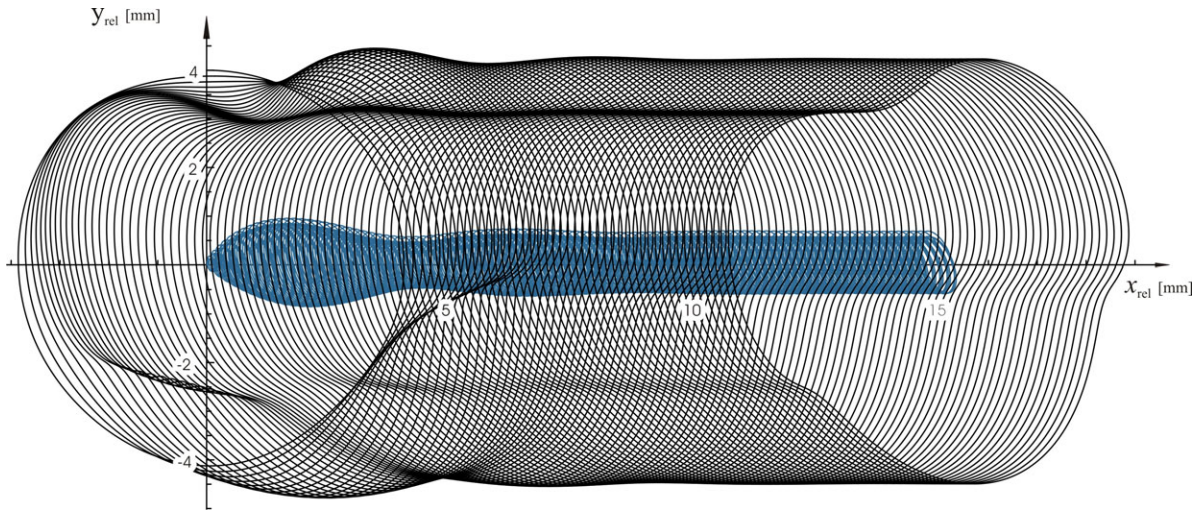

Figure 21: Tooth edge and tool centre path relative to the work-piece by time domain simulation. Parameters are $Z = 1$, $\Omega = 1125[rad/s]$, $w = 0.4[mm]$, $f_z = 0.15[mm]$, $a_{ep} = 1.5$.

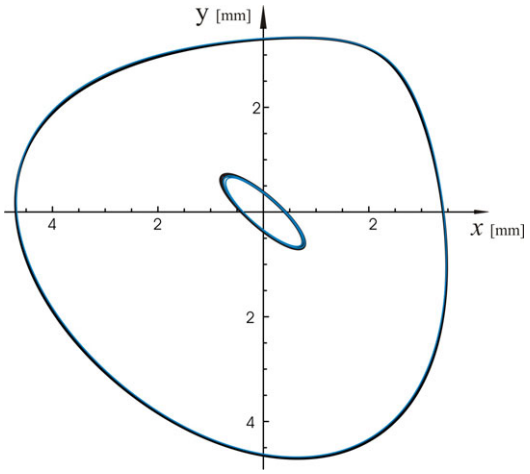

Figure 22: Motion of the tooth edge and the tool centre calculated by the analytical (blue lines) and time domain (black lines) simulation after 100 period. Parameters are $Z = 1$, $\Omega = 2250[rad/s]$, $w = 0.4[mm]$, $f_z = 0.15[mm]$, $a_{ep} = 0.5$.

3.3.3. Surface calculation

To generate the cut surface we need to find the motion of the edges relative to the work-piece. By using (77) motion of the edge relative to the feed motion (v) is given by

$$\mathbf{e}_{rel}(t) = \mathbf{e}(t) + \begin{bmatrix} vt \\ 0 \end{bmatrix}. \tag{79}$$

If we use a tool with more than one tooth all the edge paths are the same, but there are shifts in the x direction between the paths: the distance between two neighbouring path is the feed per tooth. In case of up-milling the surface is defined by the curve which bounds these paths from above. In down-milling it is shaped by the lower bounding curve (see figure 23).

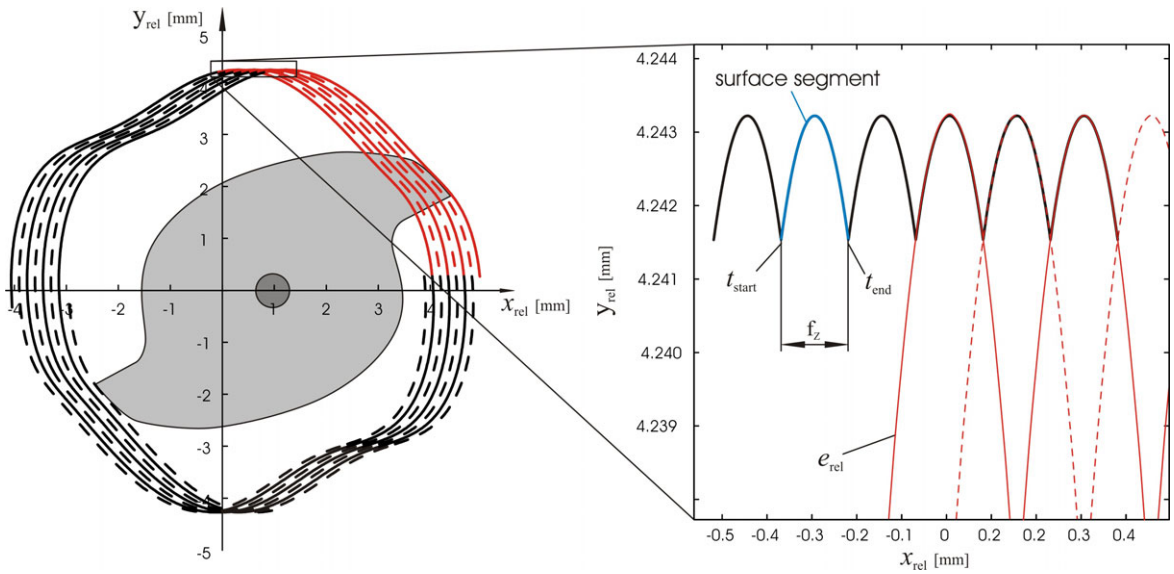

Figure 23: Surface is defined by the relative motions of the edges in up-milling process. Solid lines belongs to the first tooth, dash lines belongs to the second tooth. Parameters are $Z = 2$, $\Omega = 450[rad/s]$, $w = 0.4[mm]$, $f_z = 0.15[mm]$, $a_{ep} = 0.5$.

Figure 23 shows clearly that the surface can be described with a single piece of surface segment. Assuming periodicity one representative segment form the surface, $\mathbf{s}(t)$, can be described as a part of (79) between t_{start} and t_{end} so

$$\mathbf{s}(t) = \begin{bmatrix} x_{surf}(t) \\ y_{surf}(t) \end{bmatrix} = \mathbf{e}_{rel}(t) \qquad t \in [t_{start}, t_{end}]. \tag{80}$$

We have to determine the times (t_{start}, t_{end}), when the edge is on the boundary of the surface segment. The two unknown times can be determined from (81) by using that fact the width of the segment is f_Z:

$$\mathbf{e}_{rel}(t_{start,i}) + \begin{bmatrix} f_z \\ 0 \end{bmatrix} = \mathbf{e}_{rel}(t_{end,i}). \tag{81}$$

There are several solutions of this equation, but only one pair is needed. The solutions of (81) are repeated periodically, with period *T*. We can choose any such pair of these solutions, because they produce the same surface, and hence we can neglect the multiple solutions. We must use that pair which is closest to the surface. In the case of up-milling it must be the highest intersection point

$$\begin{aligned} t_{\text{start}} &:= t_{\text{start},k} \quad \text{where} \quad y_{\text{surf}}(t_{\text{start},k}) = \max_i \left(y_{\text{surf}}(t_{\text{start},i}) \right) \\ t_{\text{end}} &:= t_{\text{end},k} \quad \text{where} \quad y_{\text{surf}}(t_{\text{end},k}) = \max_i \left(y_{\text{surf}}(t_{\text{end},i}) \right), \end{aligned} \tag{82}$$

and for down-milling it is the lowest point, so

$$\begin{aligned} t_{\text{start}} &:= t_{\text{start},k} \quad \text{where} \quad y_{\text{surf}}(t_{\text{start},k}) = \min_i \left(y_{\text{surf}}(t_{\text{start},i}) \right) \\ t_{\text{end}} &:= t_{\text{end},k} \quad \text{where} \quad y_{\text{surf}}(t_{\text{end},k}) = \min_i \left(y_{\text{surf}}(t_{\text{end},i}) \right). \end{aligned} \tag{83}$$

Hence the surface can be described totally with this single surface segment.

We now describe two measures of the quality of the milled surface, the surface roughness, and the surface location error, illustrated schematically in figure 24. The surface roughness (μ), given by

$$\mu = \max_t \left(y_{\text{surf}}(t) \right) - \min_t \left(y_{\text{surf}}(t) \right). \tag{84}$$

On the other hand, the surface location error (SLE) is an offset error, which is the distance between the desired surface and the formed surface. In case of up-milling it is given by

$$SLE = \max_t \left(y_{\text{surf}}(t) \right) - R, \tag{85}$$

and for down-milling

$$SLE = -\min_{t}\left(y_{\text{surf}}(t)\right) - R\,. \tag{86}$$

These kind of surface errors are represented in figure 24.

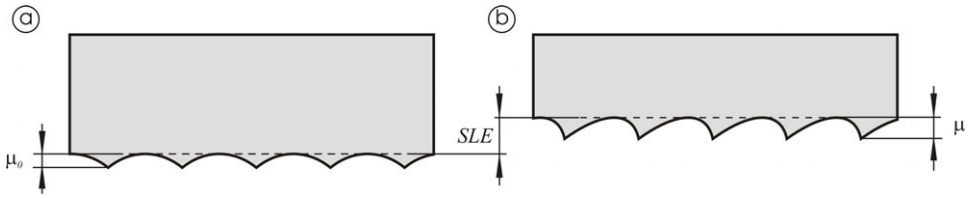

Figure 24: Schematic representation of the surface location error and the surface quality. (a) desired surface, (b) machined surface.

By using the methods which are described in chapter 4 we can calculate the stability chart of the milling process and determine the surface properties in the case of straight edged tool. This calculations were used to validate our methods and used as a base of further calculations.

4. Tool with helical edge

In practice, tool edges are always helical. Experimental evidence suggests that helical tools make smooth cut surfaces, and that they make the function of force less ‘impact-like’ and hence make a smaller load for the machine-tool. From the point of view of theoretical approaches, in [11] the tool was sliced into finite segments, each described as a tool with straight edge. The cutting force was approach as a sum of the cutting force acting on each segment. The quality of this approximation strongly depends on the number of the segments.

In our calculation we use a continuous model and use the exact cutting force.

4.1. Equation of motion

The system can be described in the same way as in the straight edge model; in the helical model the angular position of the tooth edge, ϕ_j, depends on the vertical coordinate (z), which is parallel to the axis of the tool

$$\phi_j(z,t) = t\Omega + j\frac{2\pi}{Z} - \frac{2\pi z}{p}, \tag{87}$$

where p is the helix pitch and Z is the number of teeth as before (see figure 25).

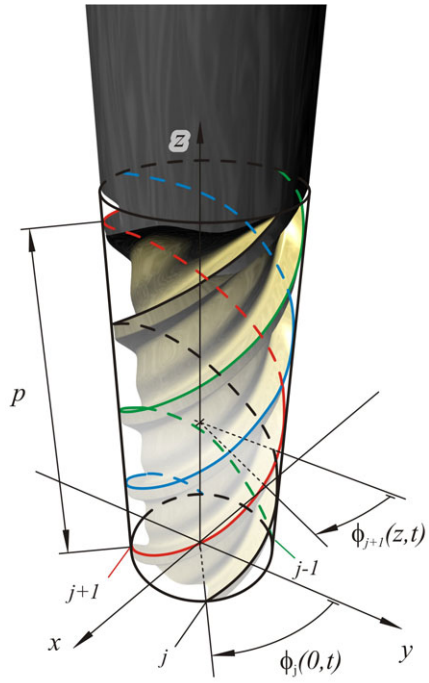

Figure 25: Helix pitch and angular position of the edge as a function of the *z* coordinate.

Due to the helical edge we have to change the calculation of the cutting force. In a cross section of the tool the cutting force can calculated in the same way as in the straight edge model with an infinitesimally small chip width (dz). We can calculate the cutting force by integrating this equation, so

$$\mathbf{F}(t) = \sum_{j=0}^{Z-1} \int_{z=0}^{w} g_j\left(\phi_j(z,t)\right)\left(\mathbf{F}_j^{t}(t) + \mathbf{F}_j^{r}(t)\right) dz\,. \tag{88}$$

Following the method of calculation in section 3.1, we get a similar equation to (24) for the cutting force in terms of the system states

$$\mathbf{F}(t) = \tilde{\mathbf{W}}(t)\left(\begin{bmatrix} f_z \\ 0 \end{bmatrix} + \mathbf{q}(t) - \mathbf{q}(t-\tau)\right), \tag{89}$$

where $\tilde{\mathbf{W}}(t)$ is the periodic excitation matrix for the helical tool, given by

$$\widetilde{\mathbf{W}}(t)=\sum_{j=0}^{Z-1}\widetilde{\mathbf{W}}_j(t)=\sum_{j=0}^{Z-1}\int_{z=0}^{w}\frac{k_t}{2}g_j\left(\phi_j(z,t)\right)\mathbf{T}\left(\phi_j(z,t)\right)dz\,. \tag{90}$$

The limit of integration can be changed simply to the angular coordinate (see figure 26.) because the function $\phi_j(z,t)$ is linear, so

$$\widetilde{\mathbf{W}}(t)=\sum_{j=0}^{Z-1}\int_{\phi_j(t,w)}^{\phi_j(t,0)}\frac{k_t\,p}{4\pi}g_j\left(\phi_j(z,t)\right)\mathbf{T}\left(\phi_j(z,t)\right)d\phi\,. \tag{91}$$

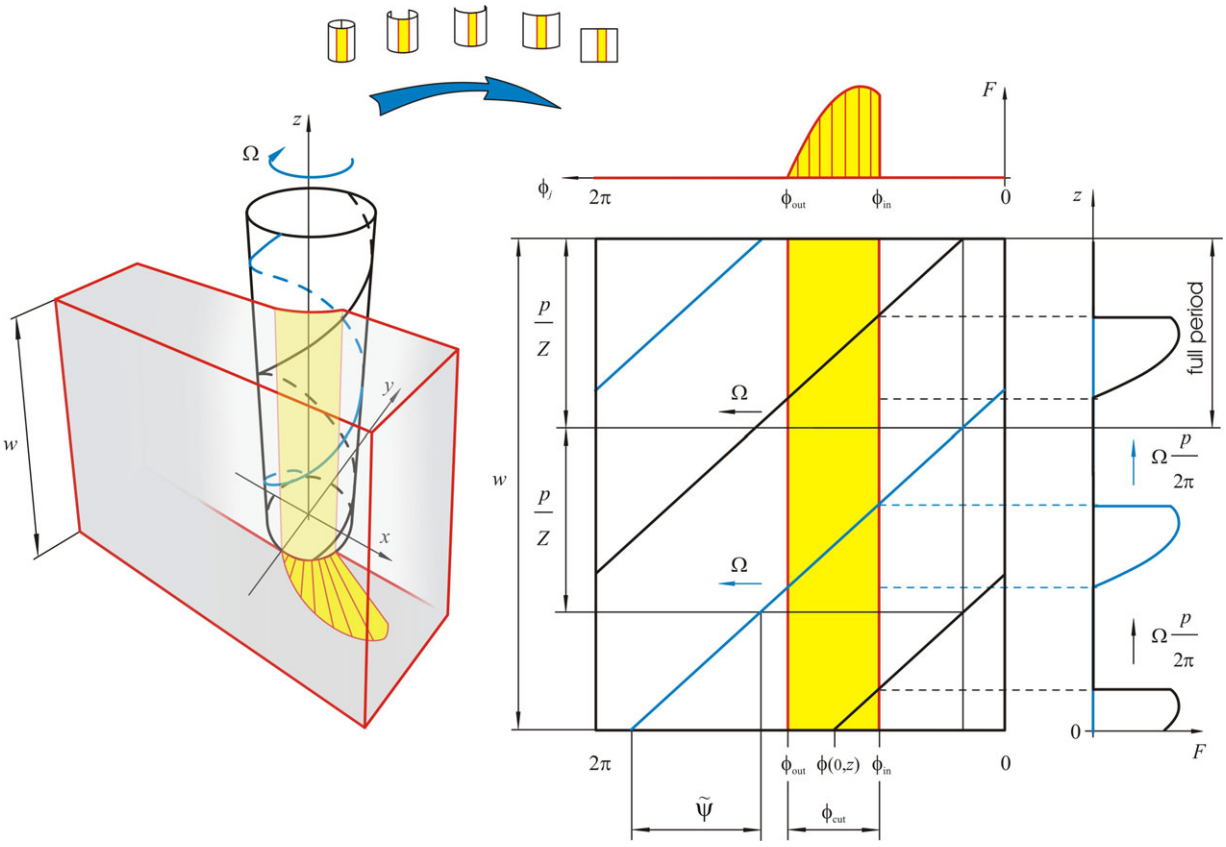

Figure 26: Integration of the cutting force along the helical edge in two fluted tool.

Figure 26 shows clearly that if the angle of the helical edge satisfies

$$\psi := \phi_j(0,t) - \phi_j(w,t) > \frac{2\pi}{Z}, \tag{92}$$

then the integration (91) comprises two parts. The first contains those sections of the integration where we integrate on a full period (see figure 26). This part is constant in time. If the axial immersion is large enough, then it can contain more then one full period. The number of the full period is given by

$$N_{\text{full}} = \text{int}\left(\frac{\left(\phi_j(0,t) - \phi_j(w,t)\right)Z}{2\pi}\right), \tag{93}$$

where $\text{int}(x)$ is the largest integer $\le x$.

The result of the integration of a section ($\overline{\mathbf{W}}$) can be calculated as an integration between ϕ_{in} and ϕ_{out} by using the definition of the g_j function (10), so

$$\overline{\mathbf{W}} = \int_0^{2\pi} \frac{k_t\, p}{4\pi} g_j\left(\phi_j(z,t)\right)\mathbf{T}\left(\phi_j(z,t)\right)d\phi = \int_{\phi_{\text{in}}}^{\phi_{\text{out}}} \frac{k_t\, p}{4\pi}\mathbf{T}\left(\phi_j(z,t)\right)d\phi\,, \tag{94}$$

where ϕ_{in} and ϕ_{out} are the angular position for which cutting begins and finishes respectively (see (11) and (12)).

Another part of (91) contains the rest of the integration. The length of this integration is given by

$$\widetilde{\psi} = \psi - \frac{2\,\pi\, N_{\text{full}}}{Z}. \tag{95}$$

Hence we can write (91) as

$$\widetilde{\mathbf{W}} = N_{\text{full}}\overline{\mathbf{W}} + \sum_{j=0}^{Z-1} \mathbf{W}_j \ , \tag{96}$$

where

$$\mathbf{W}_j = \int_{\phi_j(t,0)-\tilde{\psi}}^{\phi_j(t,0)} \frac{k_t\, p}{4\pi} g_j\left(\phi_j(z,t)\right)\mathbf{T}\left(\phi_j(z,t)\right)d\phi \ . \tag{97}$$

To eliminate g_j from $\mathbf{W}_j$ we have to use new integration limits (a_j, b_j), which are time dependent, so

$$\mathbf{W}_j = \int_{a_j(t)}^{b_j(t)} \frac{k_t\, p}{4\pi} \mathbf{T}\left(\phi_j(z,t)\right)d\phi \ . \tag{98}$$

There are three different cases in calculating a_j and b_j according to the length of $\tilde{\psi}$. The three cases are represented in figure 27. The lengths of the cutting and flying phases are given by

$$\phi_{\text{cut}} = \phi_{\text{out}} - \phi_{\text{in}} \qquad \phi_{\text{fly}} = 2\pi - \phi_{\text{cut}} \ . \tag{99}$$

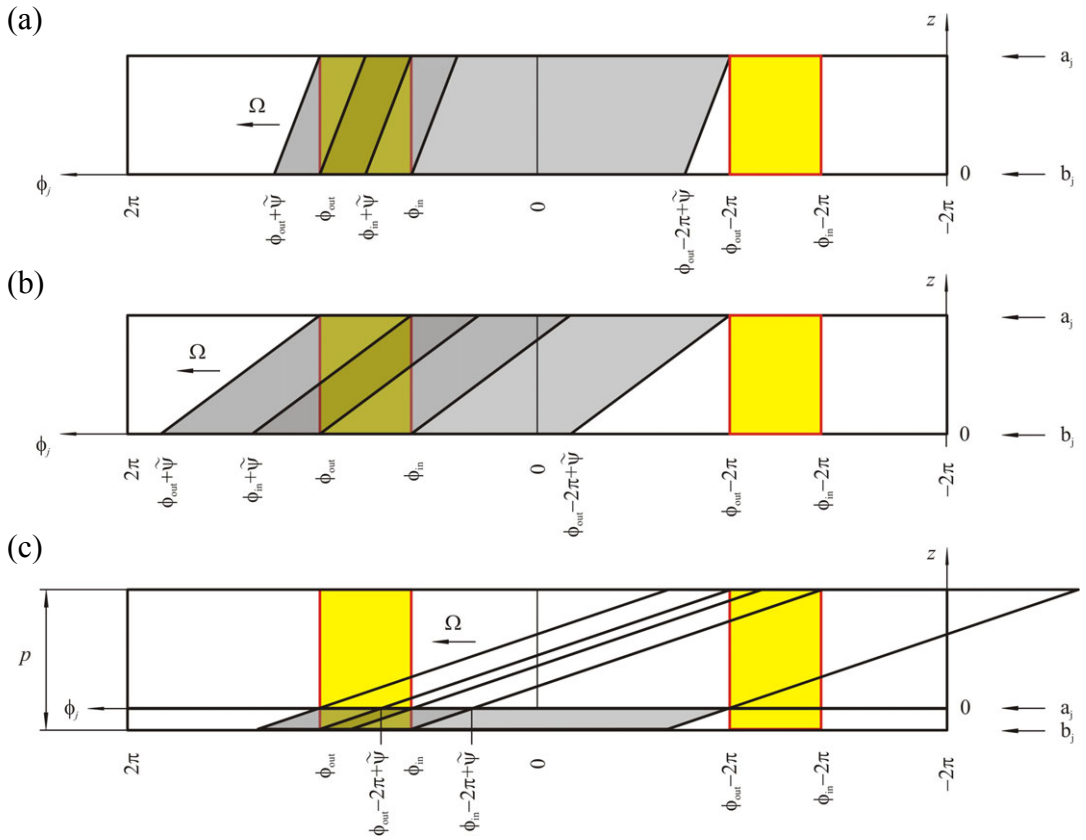

Figure 27: Graphical presentation of the integration limits of $\mathbf{W}_j$ in case $0 < \tilde{\psi} \le \phi_{\text{cut}}$ (a), $\phi_{\text{cut}} < \tilde{\psi} \le \phi_{\text{fly}}$ (b) and $\phi_{\text{fly}} < \tilde{\psi} < 2\pi$ (c). Yellow shading denotes the cutting phase.

While there is no contact between the work-piece and the helical edge $\mathbf{W}_j$ is zero.

In case (b) $\tilde{\psi}$ is bigger then the cutting phase ϕ_{cut}, for this reason sometimes the helical arc covers the whole cutting phase ϕ_{cut}. In this case we have to integrate between ϕ_{in} and ϕ_{out} as constant limits, so $\mathbf{W}_j$ is constant for this period.

The limits of integration (a_j, b_j) are presented in table 2. If we use a cyclical coordinate

$$\phi_j' = (\phi_j - \tilde{\psi} - \phi_{\text{out}} \bmod 2\pi) + \tilde{\psi} + \phi_{\text{out}} - 2\pi \qquad \phi_j' \in [\tilde{\psi} + \phi_{\text{out}} - 2\pi, \tilde{\psi} + \phi_{\text{out}}[. \qquad (100)$$

instead of the total angle ϕ_j, then we can make a simpler notation.

In case (c) we can make an easier calculation by filling the helical arc to 2π and then subtraction this part from $\overline{\mathbf{W}}$ (94), so

$$\mathbf{W}_j = \overline{\mathbf{W}} - \int_{a_j'(t)}^{b_j'(t)} \frac{k_t\, p}{4\pi} \mathbf{T}\big(\phi_j(z,t)\big) d\phi \ , \tag{101}$$

and using a different domain for ϕ_j', given by

$$\phi_j' = \mathrm{mod}(\phi_j - \phi_{\mathrm{out}} + 2\pi, 2\pi) + \phi_{\mathrm{out}} - 2\pi \qquad \phi_j' \in \left[\phi_{\mathrm{out}} - 2\pi, \phi_{\mathrm{out}}\right). \tag{102}$$

(a)

Type	Part	$a_j(t)$	$b_j(t)$
Fly	$\widetilde{\psi} + \phi_{\mathrm{out}} - 2\pi < \phi_j'(0,t) \le \phi_{\mathrm{in}}$	$\mathbf{W}_j = \mathbf{0}$	
Step in	$\phi_{\mathrm{in}} < \phi_j'(0,t) \le \phi_{\mathrm{in}} + \widetilde{\psi}$	ϕ_{in}	$\phi_j'(0,t)$
Inside	$\phi_{\mathrm{in}} + \widetilde{\psi} < \phi_j'(0,t) \le \phi_{\mathrm{out}}$	$\phi_j'(0,t) - \widetilde{\psi}$	$\phi_j'(0,t)$
Step out	$\phi_{\mathrm{out}} < \phi_j'(0,t) \le \phi_{\mathrm{out}} + \widetilde{\psi}$	$\phi_j'(0,t) - \widetilde{\psi}$	ϕ_{out}

(b)

Type	Part	$a_j(t)$	$b_j(t)$
Fly	$\widetilde{\psi} + \phi_{\mathrm{out}} - 2\pi < \phi_j'(0,t) \le \phi_{\mathrm{in}}$	$\mathbf{W}_j = \mathbf{0}$	
Step in	$\phi_{\mathrm{in}} < \phi_j'(0,t) \le \phi_{\mathrm{out}}$	ϕ_{in}	$\phi_j'(0,t)$
Cover	$\phi_{\mathrm{out}} < \phi_j'(0,t) \le \phi_{\mathrm{in}} + \widetilde{\psi}$	ϕ_{in}	ϕ_{out}
Step out	$\phi_{\mathrm{in}} + \widetilde{\psi} < \phi_j'(0,t) \le \phi_{\mathrm{out}} + \widetilde{\psi}$	$\phi_j'(0,t) - \widetilde{\psi}$	ϕ_{out}

(c)

Type	Part	$a_j(t)$	$b_j(t)$
Fly	$\phi_{\mathrm{out}} - 2\pi < \phi_j'(0,t) \le \phi_{\mathrm{in}} - 2\pi + \widetilde{\psi}$	$\mathbf{W}_j = \mathbf{0}$	
Step in	$\phi_{\mathrm{in}} - 2\pi + \widetilde{\psi} < \phi_j'(0,t) \le \phi_{\mathrm{in}}$	ϕ_{in}	$\phi_j'(0,t) + 2\pi - \widetilde{\psi}$
Inside	$\phi_{\mathrm{in}} < \phi_j'(0,t) \le \phi_{\mathrm{out}} - 2\pi + \widetilde{\psi}$	$\phi_j'(0,t)$	$\phi_j'(0,t) + 2\pi - \widetilde{\psi}$
Step out	$\phi_{\mathrm{out}} - 2\pi + \widetilde{\psi} < \phi_j'(0,t) \le \phi_{\mathrm{out}}$	$\phi_j'(0,t)$	ϕ_{out}

In case (a) $0 \le \widetilde{\psi} < \phi_{\mathrm{cut}}$, case (b) $\phi_{\mathrm{cut}} \le \widetilde{\psi} < \phi_{\mathrm{fly}}$, case (c) $\phi_{\mathrm{fly}} \le \widetilde{\psi} < 2\pi$.

Table 2: The integration limits of $\mathbf{W}_j$.

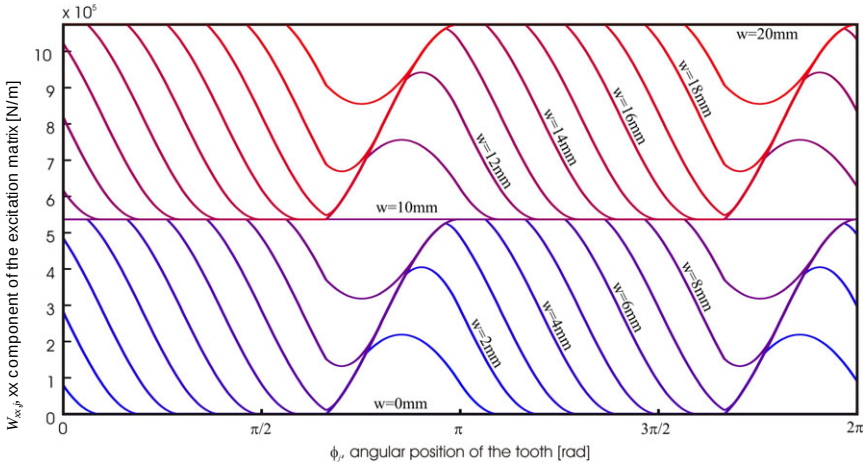

Figure 28: Function of $W_{xx\,j}$ in different axial immersion.

Parameters are $Z = 2$, $p = 20[mm]$.

These manipulations allow us to compute the periodic excitation matrix $\widetilde{\mathbf{W}}$. Using an analogous method to that presented in section 3.1, we split the solution into two parts, one a linear 2nd order ODE

$$\mathbf{M}\ddot{\mathbf{x}}(t) + \mathbf{K}\dot{\mathbf{x}}(t) + \mathbf{S}\mathbf{x}(t) = \widetilde{\mathbf{W}}(t)\begin{bmatrix} f_z \\ 0 \end{bmatrix} = \widetilde{\mathbf{f}}(t), \tag{103}$$

and the other a linear 2nd order DDE

$$\mathbf{M}\ddot{\boldsymbol{\xi}}(t) + \mathbf{K}\dot{\boldsymbol{\xi}}(t) + \left(\mathbf{S} - \widetilde{\mathbf{W}}(t)\right)\boldsymbol{\xi}(t) = -\widetilde{\mathbf{W}}(t)\boldsymbol{\xi}(t-\tau). \tag{104}$$

4.2. Stability

The stability of the system described by (104) can be calculated with the same semi-discretization method described in section 3.2.2. Note that we can describe the straight edge tool by using an infinite helix pitch ($p = \infty$). By using a very large helix pitch ($p = 1[m]$) we get the same stability chart as for the straight edge tool, validating our numerics.

Periodic chatter is caused by the flip bifurcation that occurs due to the parametric excitation. If ψ is zero, we have that

$$w = k\frac{p}{Z} \qquad k \in \mathbb{N}^+, \tag{105}$$

so the excitation matrix is constant, and there is no parametric excitation. Hence, along such line in parameter space there can be no flip bifurcation and the stability boundaries are the some as in the zeroth order approximation (see section 3.2). For a straight edged tool it is proved in [12] that the flip bifurcation boundaries are closed curves (called lenses or islands) in the stability chart on every lobe except the first one. In the first lobe the period doubling boundary is not a closed curve. If we use a helical tool, lenses can be found in every lobe (shown in figure 29); the same phenomenon was observed in shown in [13].

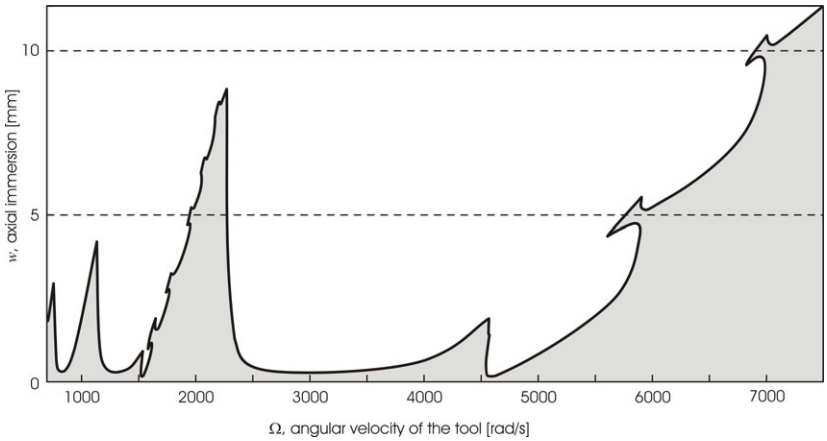

Figure 29: Period doubling islands in the first lobe caused by the helical edge.

Parameters are $Z = 2$, $a_{ep} = 0.05$, $p = 10[mm]$.

4.3. Motion of the tool centre

We could calculate the vibration of the tool centre analytically from equation (103) in a similar fashion the straight edge model (see section 3.3.1.). This method assumes that only one edge is cutting. However this assumption is good only in a small region of the parameter space; it is valid if

$$Z \le \frac{2\pi}{\phi_{out} + \psi - \phi_{in}}. \tag{106}$$

We can see that this is only valid in the case of small axial immersion, or large helix pitch. This small parameter region is also contains three different cases of calculation method due to the fact that $\mathbf{W}_j$ is a non-smooth function of *w* too. So the analytical method is, in practice, too difficult to use in the general case. For this reason we solve the particular solution of (103) by using the firs N_F terms of Fourier series of $\tilde{\mathbf{f}}$ (53). During the calculations the first 25 terms were used ($N_F = 25$).

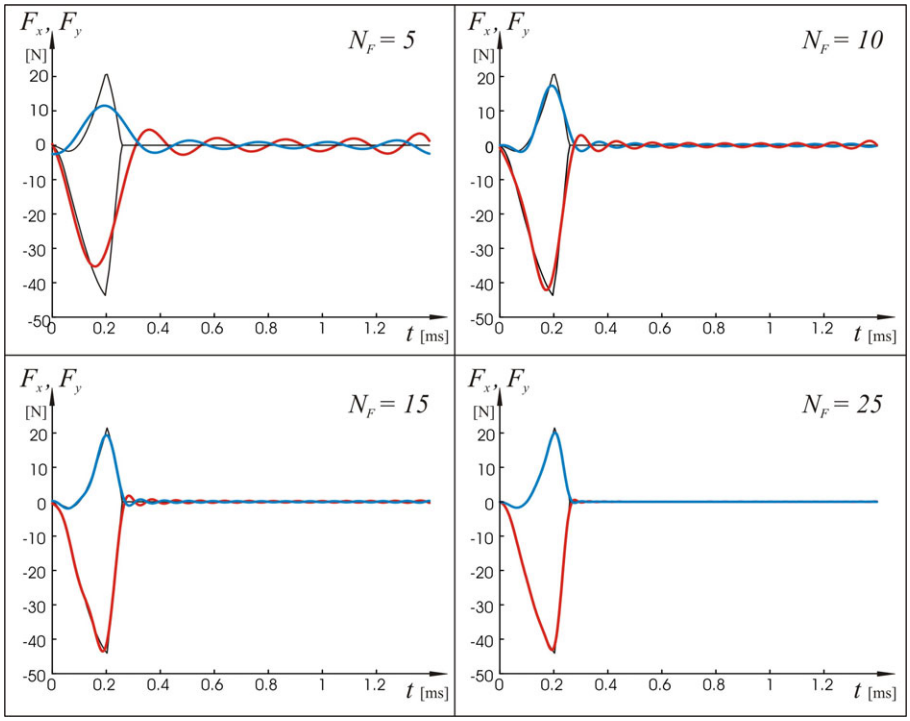

Figure 30: Excitation force and its Fourier approximation. Red lines denote the *x* component; blue lines denote the *y* component of the approximated force. Black lines denote the components of the exact force. Parameters are $Z = 1$, $\Omega = 4500[rad/s]$, $w = 1[mm]$, $f_z = 0.1[mm]$, $p = 25[mm]$, $a_{ep} = 0.2$.

In this method the particular solution of the tool-centre vibration is also given by a series of trigonometric functions (54) (as in section 3.3). Using this solution the motion of the edge $\mathbf{e}(z,t)$ can be described by superposing this vibration on a cylinder. This cylinder is created by the edge of the rigid tool

$$\mathbf{e}(z,t) = \mathbf{e}_j(z,t) = \begin{bmatrix} x(t) \\ y(t) \end{bmatrix} + \begin{bmatrix} R\cos(\phi_j(z,t)) \\ R\sin(\phi_j(z,t)) \end{bmatrix}. \tag{107}$$

The vibration and the circular motion of the edges is parallel to the *x*-*y* plane, the sides of cylinder are parallel to the *z* axis. In spite of these symmetries the surface $\mathbf{e}(z,t)$, where the edge is moving does not have regularity because we superpose the vibration onto the cylinder at the appropriate phase according to the helix angle which causes the deformation.

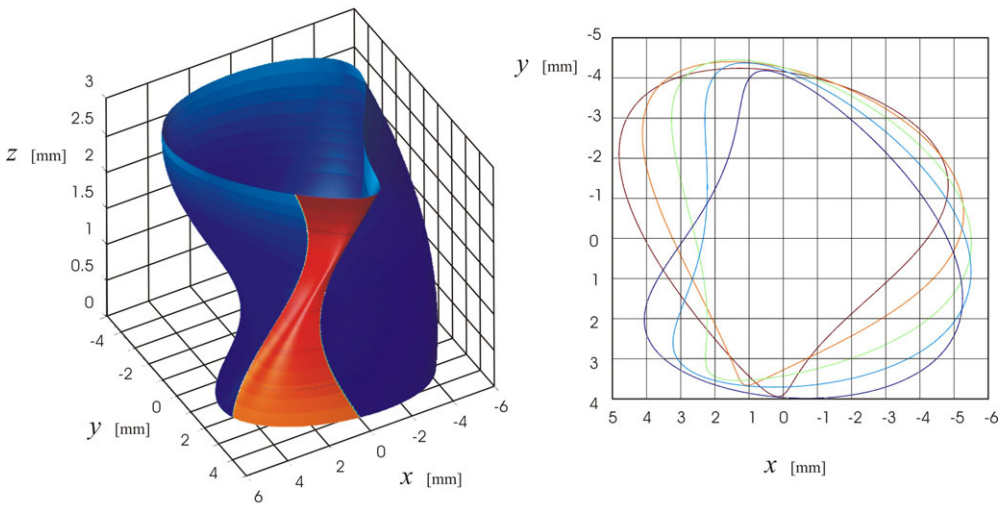

Figure 31: Path of the helical edge and its section.

Red surfaces denote the cutting phase, blue surfaces denote the flying phase.

Parameters are $Z=1$, $\Omega=2270[rad/s]$, $w=3[mm]$, $f_z=0.1[mm]$, $p=10[mm]$, $a_{ep}=0.2$.

4.4. Surface calculation

To describe the surface we have to follow the calculation between (79) and (86), but in this case all the variables are a function of the *z* coordinate. The motion of the edge relative to the surface is given by

$$\mathbf{e}_{\text{rel}}(z,t)=\mathbf{e}(z,t)+\begin{bmatrix} vt \\ 0 \end{bmatrix}. \tag{108}$$

We have to determine the lines $(t_{\text{start}}(z),t_{\text{end}}(z))$, when the edge is on the boundary of the surface segment. These lines can be calculated from.

$$\mathbf{e}_{\text{rel}}(z,t_{\text{start},i}(z))+\begin{bmatrix} f_z \\ 0 \end{bmatrix}=\mathbf{e}_{\text{rel}}(z,t_{\text{end},i}(z)). \tag{109}$$

We need those points along the z axis which are closest to the surface. These points can be determined for up-milling by

$$\begin{aligned} t_{\text{start}}(z) &:= t_{\text{start},k}(z) \quad \text{where} \quad y_{\text{surf}}(t_{\text{start},k}(z)) = \max_i \left(y_{\text{surf}}(t_{\text{start},i}(z)) \right) \\ t_{\text{end}}(z) &:= t_{\text{end},k}(z) \quad \text{where} \quad y_{\text{surf}}(t_{\text{end},k}(z)) = \max_i \left(y_{\text{surf}}(t_{\text{end},i}(z)) \right), \end{aligned} \tag{110}$$

and for down-milling by

$$\begin{aligned} t_{\text{start}}(z) &:= t_{\text{start},k}(z) \quad \text{where} \quad y_{\text{surf}}(t_{\text{start},k}(z)) = \min_i \left(y_{\text{surf}}(t_{\text{start},i}(z)) \right) \\ t_{\text{end}}(z) &:= t_{\text{end},k}(z) \quad \text{where} \quad y_{\text{surf}}(t_{\text{end},k}(z)) = \min_i \left(y_{\text{surf}}(t_{\text{end},i}(z)) \right), \end{aligned} \tag{111}$$

It is not necessary that these lines are continuous curves. The lines ($t_{\text{start}}(z)$ and $t_{\text{end}}(z)$) which determines the boundary of a surface segment consists of parts of different section lines. In figure 32 we use extreme parameters to show this phenomenon more clearly.

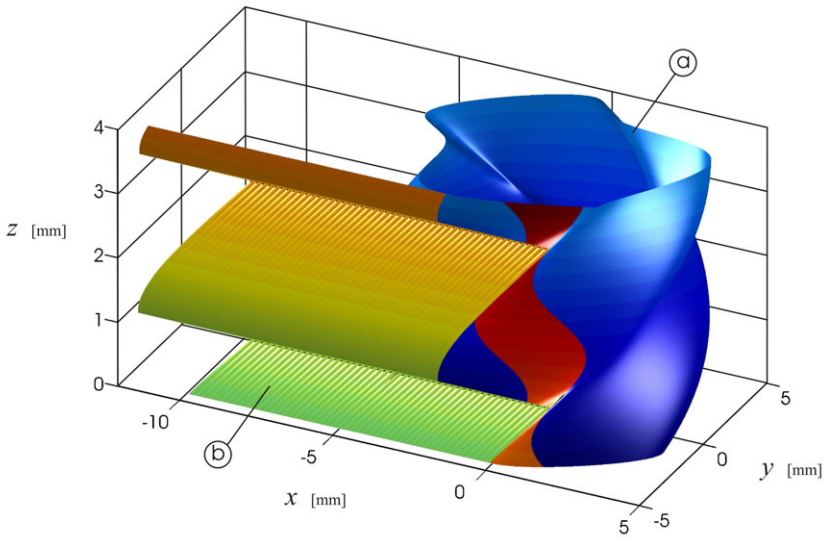

Figure 32: Surface segment boundaries formed by parts of different section lines. Blue and red surfaces denote the motion of the edge (a), yellow surfaces (b) denotes milled surface. Parameters are $Z = 2$, $\Omega = 1135[rad/s]$, $w = 4[mm]$, $f_z = 0.2[mm]$, $a_{\text{ep}} = 1.95$, $p = 10[mm]$.

Thus we can describe the surface segment by

$$\mathbf{s}(z,t)=\begin{bmatrix} x_{\text{surf}}(z,t) \\ y_{\text{surf}}(z,t) \end{bmatrix}=\mathbf{e}_{\text{rel}}(z,t) \qquad t\in\left[t_{\text{start}}(z),t_{\text{end}}(z)\right]. \tag{112}$$

We can calculate the surface roughness $\mu(z)$ by

$$\mu(z)=\max_t\left(y_{\text{surf}}(z,t)\right)-\min_t\left(y_{\text{surf}}(z,t)\right), \tag{113}$$

where the result of $\max_t$ / $\min_t$ is the maximum / minimum of the argument just along the *t* variable. In case of up-milling the surface location error is given by

$$SLE(z)=\max_t\left(y_{\text{surf}}(z,t)\right)-R, \tag{114}$$

and for down-milling

$$SLE(z)=-\min_t\left(y_{\text{surf}}(z,t)\right)-R. \tag{115}$$

However we need some single parameter to describe the surface quality rather than functions of *z*. In practice the surface quality is described by the largest difference between the points of the surface. Using a tool with a helical edge there are two different deflections. The first is in the *x* direction, which is similar to surface roughness at the straight edge model. The second is in the *z* direction due to the changing SLE. This error is caused only by the helical edge, and hence always zero in the case of a straight edged tool. In real parameter space the change of SLE is at least ten times bigger then the error in the *x* direction and the wavelength of its repetition is of the order of the helix pitch (see chapter 5.2). For this reason it is not really a surface roughness but a surface waviness. Due to this fact, the surface roughness was separated into two parts. The first is the maximum of the deflection along the *x* direction:

$$\mu_x=\max_z(\mu(z)). \tag{116}$$

The second one is the waviness of the surface, given by

$$\tilde{\mu} = \max_{z}\left(SLE(z)\right) - \min_{z}\left(SLE(z)\right). \tag{117}$$

To describe the surface location error the average of $SLE(z)$ was used, so

$$SLE = \frac{1}{w}\int_{0}^{w} SLE(z)\,dz\,. \tag{118}$$

These types of surface errors are represented graphically in figure 33.

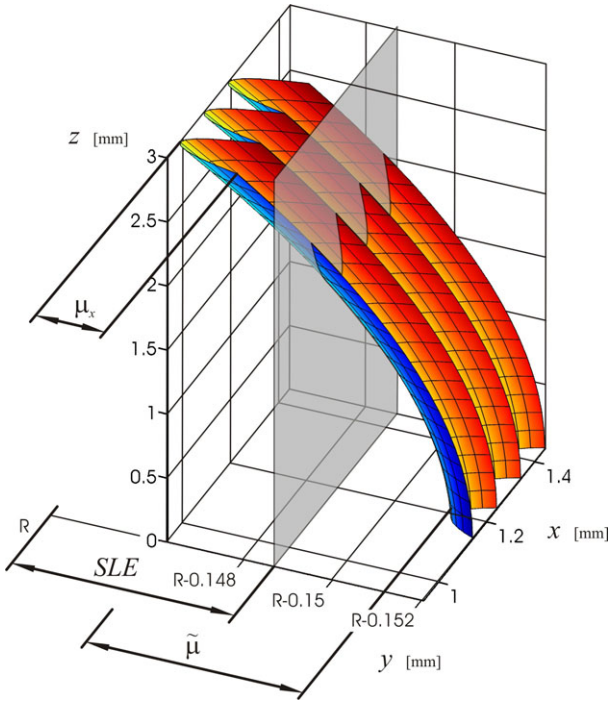

Figure 33: Schematic representation of the surface errors made by a helical tool, where R is the radius of the tool. Parameters are $Z = 1$, $\Omega = 2270[rad/s]$, $w = 3[mm]$, $f_z = 0.1[mm]$, $a_{ep} = 0.1$, $p = 150[mm]$.

5. Investigated model

To describe the effect of the parameters on the surface quality we choose a particular machine-tool and work-piece. The machine-tool is described by the same modal parameters as used in [1]. These parameters were determined experimentally. The mass (**M**), damping (**K**) and the stiffness (**S**) matrices were determined thorough modal analysis by a standard impact test procedure.

$$\mathbf{M} = \begin{pmatrix} m_x & 0 \\ 0 & m_y \end{pmatrix} = \begin{pmatrix} 0.01986 & 0 \\ 0 & 0.02008 \end{pmatrix} [kg],$$

$$\mathbf{K} = \begin{pmatrix} k_x & 0 \\ 0 & k_y \end{pmatrix} = \begin{pmatrix} 1.60312 & 0 \\ 0 & 1.155697 \end{pmatrix} \left[\frac{Ns}{m} \right],$$

$$\mathbf{S} = \begin{pmatrix} s_x & 0 \\ 0 & s_y \end{pmatrix} = \begin{pmatrix} 408\,866 & 0 \\ 0 & 413\,445 \end{pmatrix} \left[\frac{N}{m} \right].$$

The average tool diameter is between 2mm and 25mm, though a tool with inserts usually has a larger diameter between 12mm and 100mm. During the calculations we use tools with an ordinary diameter (D=8 mm).

The chosen material of the work-piece is AlMgSi0.5 aluminium alloy. It can be described by the tangential cutting coefficient (k_t) and the non-dimensional force ratio (k_r)

$$k_{\mathrm{t}} = 644 \cdot 10^6 \left[\frac{N}{m^2} \right],$$

$$k_{\mathrm{r}} = 0.368 \text{ [1].}$$

These values were determined by measurement in [14].

5.1. Stability chart

Our first task is to find regions in parameter space where tool motion is bounded. The simplest of these is where period motion exists and is stable. Then we do not have to calculate the surface for those parameter regions where the motion is unstable. The stability boundaries depend on four parameters (radial immersion (a_{ep}), chip width or axial immersion (w), angular velocity of the tool (Ω) and the helix pitch (p)) and is generally plotted as a function of the angular velocity of the tool and the axial immersion (the chip width).

First we investigate the effect of varying the radial immersion. Figure 34 shows the stability chart for different radial immersions of a straight edge model ($p \to \infty$) with one tooth. A tool with one tooth is used to have an easier understanding of the milling process.

At small radial immersion we find flip bifurcations. These bifurcations occur due to the time dependent excitation matrix ($\mathbf{W}$). In the case of small radial immersion the cutting force is more impact like due to the short switching time of the step function (g).

At large radial immersion the system loses its stability at smaller axial immersion because it gets more energy form the cutting force. In this case the ratio of the cutting phase and the flying phase increases. The longer cutting phase gives more energy to the system, and reduces the flying phase which can damp the energy.

We can see that the stability lobes for up-milling and down-milling are very similar. At large radial immersion this is obvious because, in this case, the tool is cutting on almost the same region ($\phi_{\text{in}} \cong 0$, $\phi_{\text{out}} \cong \pi$). In the case of small radial immersion the cutting force is almost constant during the short cutting phase. The period of the excitation matrix is half that of the tool rotation, and so the value of the cutting force at the beginning of the cutting phase in up-milling is the some as its value at the end of the cutting phase in down-milling. Therefore the shapes of the cutting force in time are similar, which cause the similarity of the stability charts.

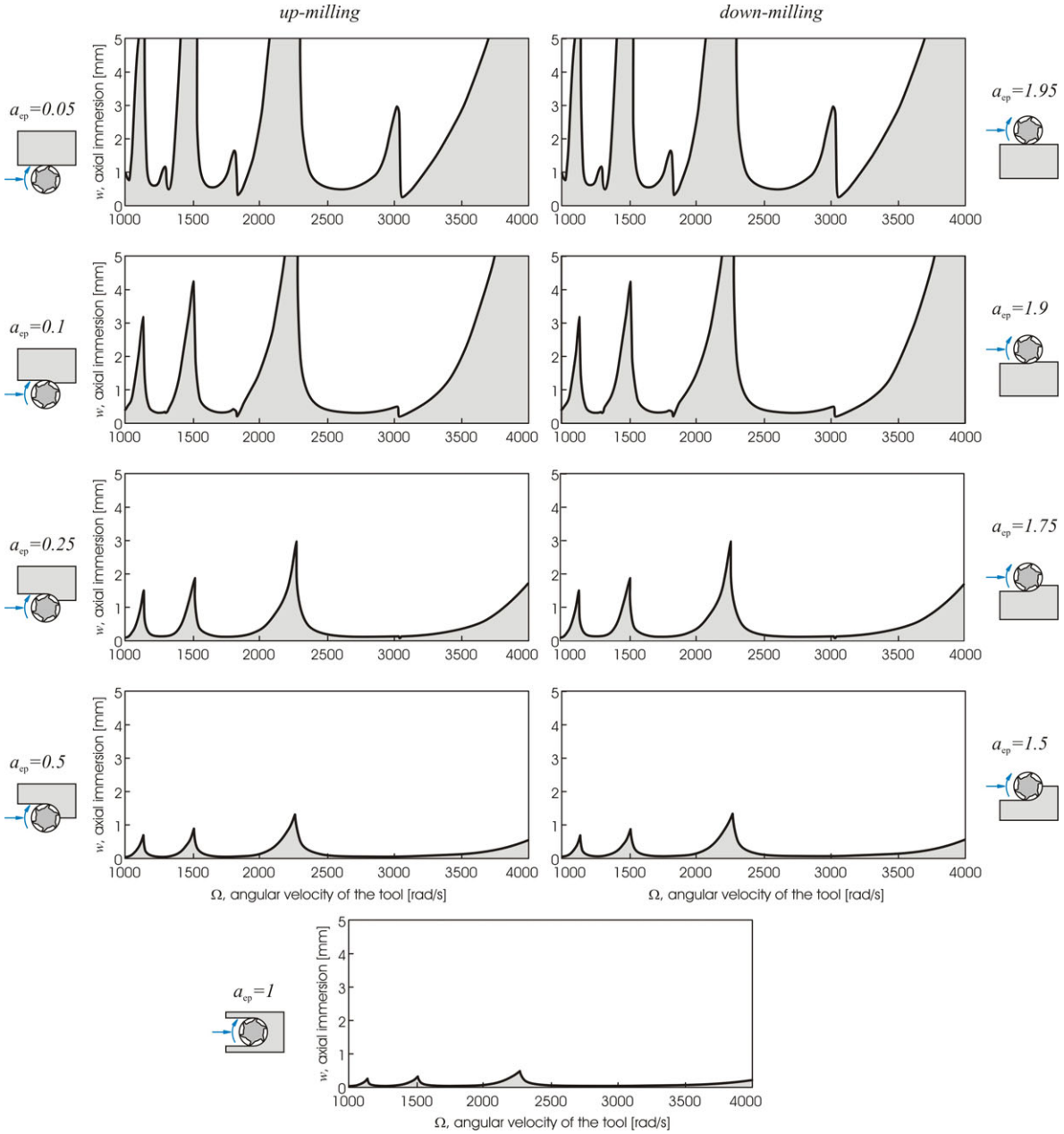

Figure 34: Stability charts for different radial immersions.

Parameters are $Z = 1$, $p \to \infty$.

Figure 35 shows the effect of the number of teeth on the stability. If we use a tool with more teeth, then the cutting phase is repeated over one revolution. This has a similar effect to multiplying the angular velocity of the tool. By using more teeth the ratio of the duration of the cutting and flying phases gets larger, which has a similar effect to a larger radial immersion, so the stable regions get smaller.

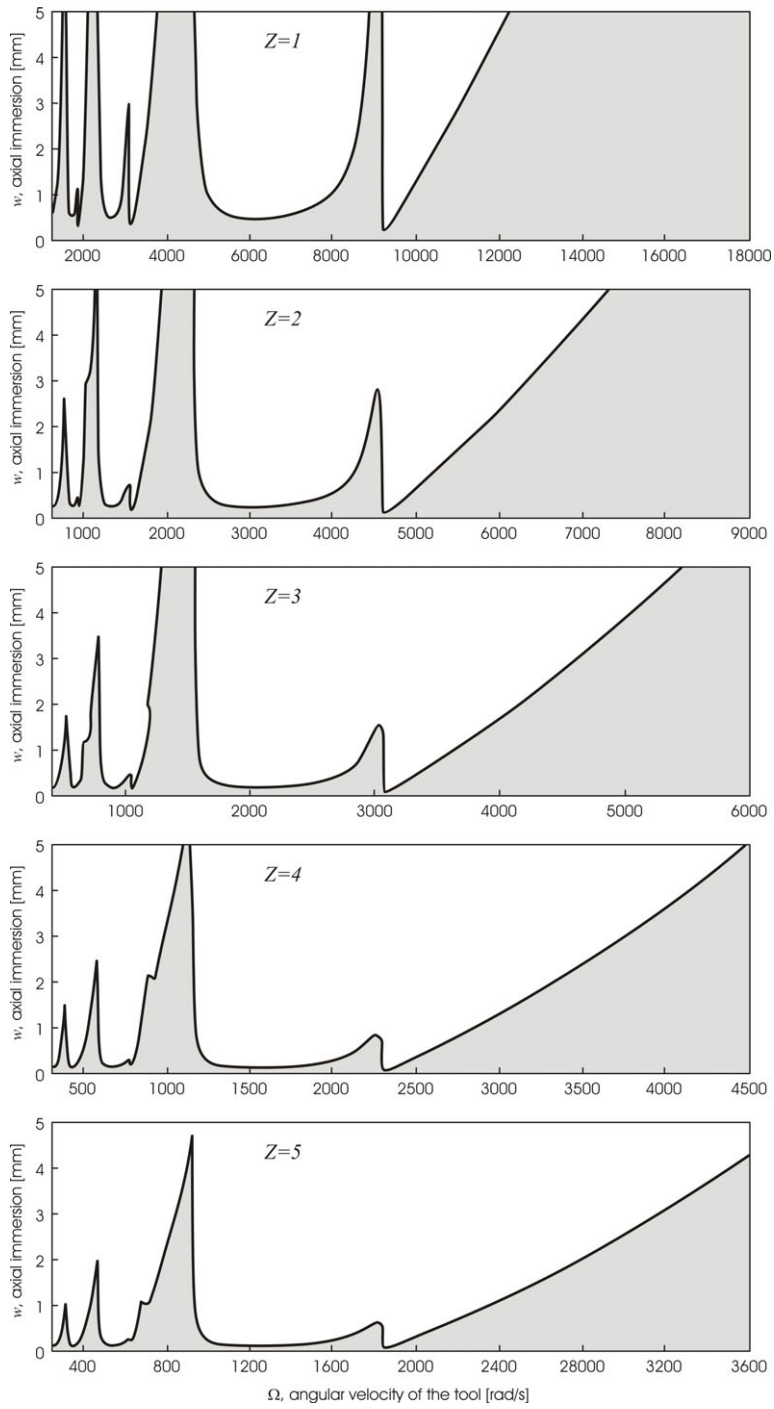

Figure 35: Stability charts for straight edge tool with different number of teeth. Note the variation of the horizontal scale of the charts. Parameters are $a_{\text{ep}} = 0.05$, $p \to \infty$.

For surface finishing (end milling) a small radial immersion is always used. For this reason we check stability lobes for different helix pitches at 5% radial immersion with 4 teeth (shown in figure 36). Again the straight-edge tool is described as a tool with infinite helix pitch. We can see that the helix pitch has a great effect on the flip bifurcation boundary. A helical tool has a smoother force in time to such an extent that the cutting force can be time

independent. The excitation matrix is constant along defined axial immersion lines (see equation (105)). Along these lines, flip bifurcations cannot occur, so the flip bifurcation curves are separated between these lines.

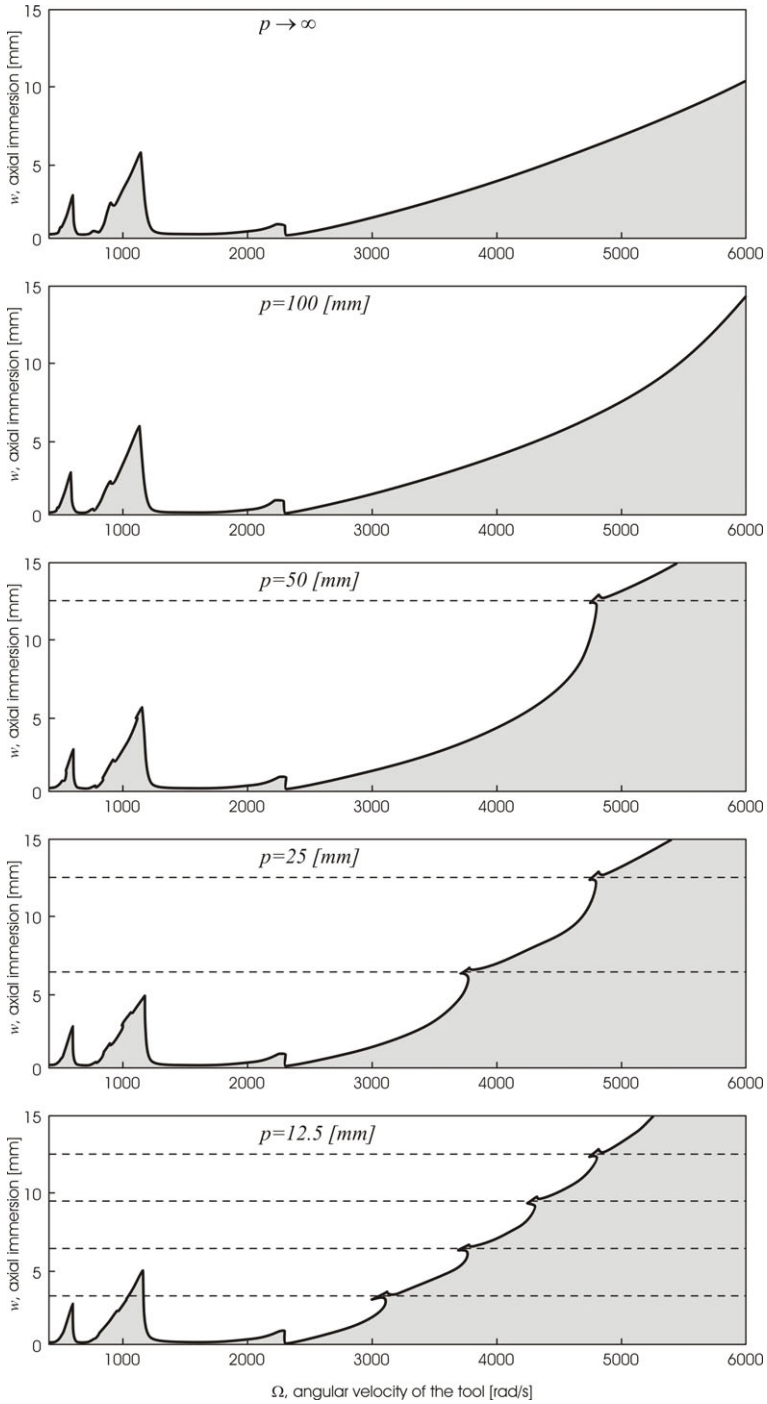

Figure 36: Stability charts for different helix pitch and small radial immersion. Along the dotted lines the excitation matrix is constant. Parameters are $Z = 4$, $a_{\mathrm{ep}} = 0.05$.

At large radial immersion there is no flip bifurcation, but only Hopf bifurcations. For this reason there is no great difference between the stability charts corresponding to different helix pitches (see figure 37).

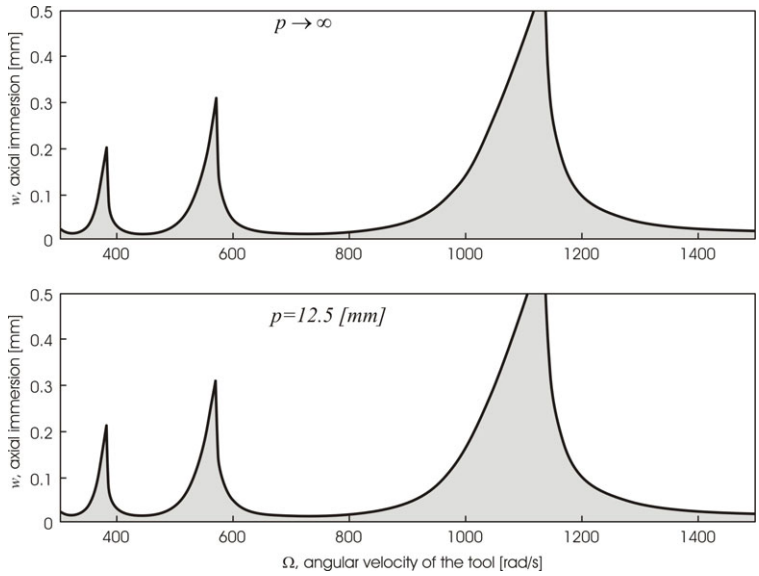

Figure 37: Stability charts for different helix pitch and half immersion up-milling.

Parameters are $Z = 4$, $a_{ep} = 0.5$.

5.2. Surface

We can now calculate the surface in parameter regions where the system is stable. The properties of the surface quality depend on the same parameters as the stability, moreover they also depend on the feed per tooth (f_z). The surface quality is important only for end milling, where a small radial immersion is typically used. Thus we made the investigation at a fixed 10% radial immersion. Figures 38 and 39 show the surface location error (SLE) (eq. (85) and (86)) and the surface roughness (μ) (eq. (84)) for up-milling, over a stability chart for a straight edge tool with a typical feed per tooth (f_z) and up-milling. Note that the surface waviness is always zero for a straight edge tool.

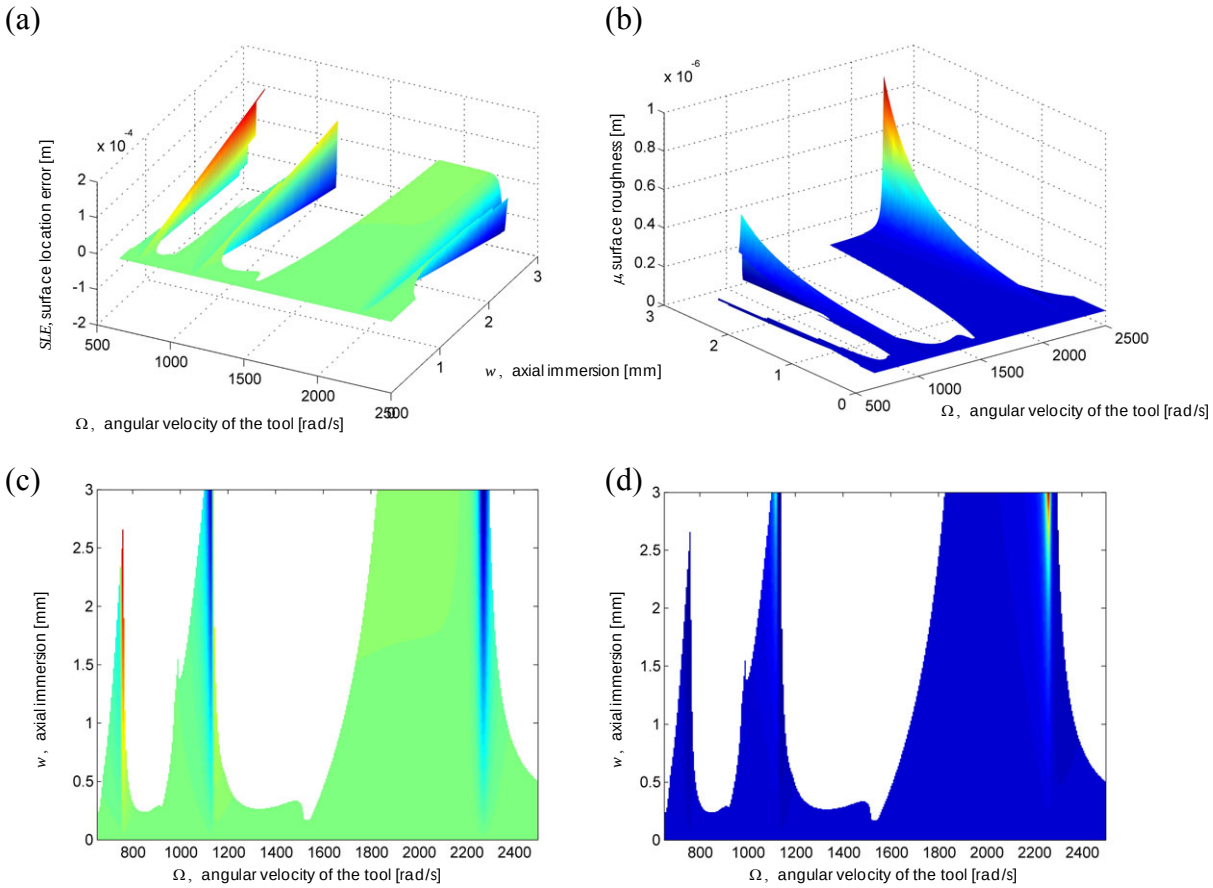

Figure 38: Surface location error (a), (c), surface roughness (b), (d)for up-milling.

Parameters are $Z = 2$, $f_z = 0.05[mm]$, $p \to \infty$, $a_{ep} = 0.1$.

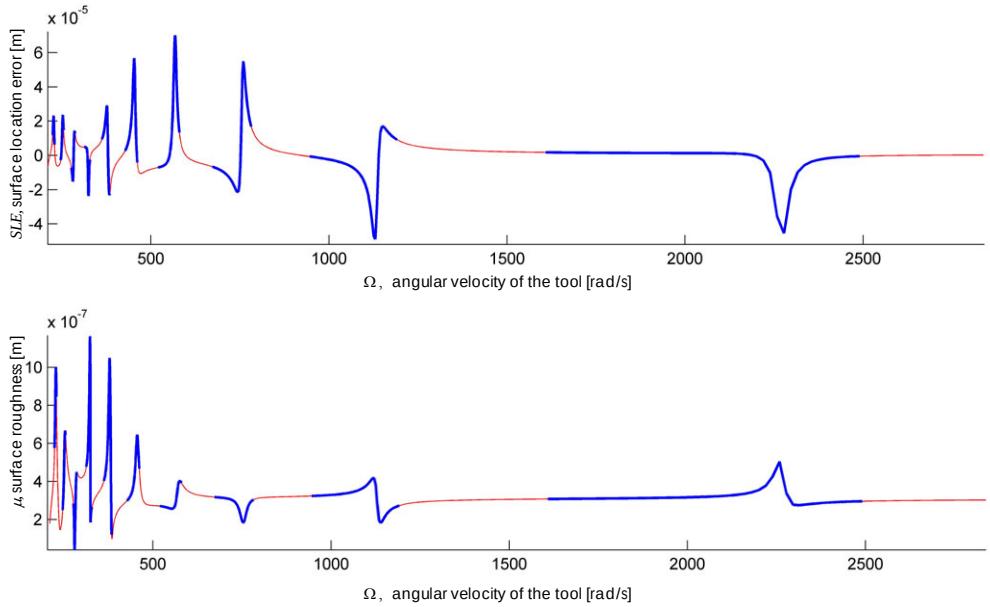

Figure 39: Surface location error, surface roughness for up-milling.

Blue lines denote stable process, red lines denote unstable process.

Parameters are $Z = 2$, $w = 0.5[mm]$, $f_z = 0.1[mm]$, $p \to \infty$, $a_{ep} = 0.1$.

We can see that there are large offset errors if we are close to on angular velocities where the ratio of the natural frequency of the system and the angular velocity is close to an integer. In this case the tool vibration is close to resonance because the frequencies of higher harmonics of the cutting force are close to the natural frequencies. The peak points of the SLE are almost proportional to the coefficient of the appropriate term of the Fourier series of the cutting force; figure 40 shows this phenomenon. The peak points of SLE do not converge evenly because of the 'impact-like' cutting force.

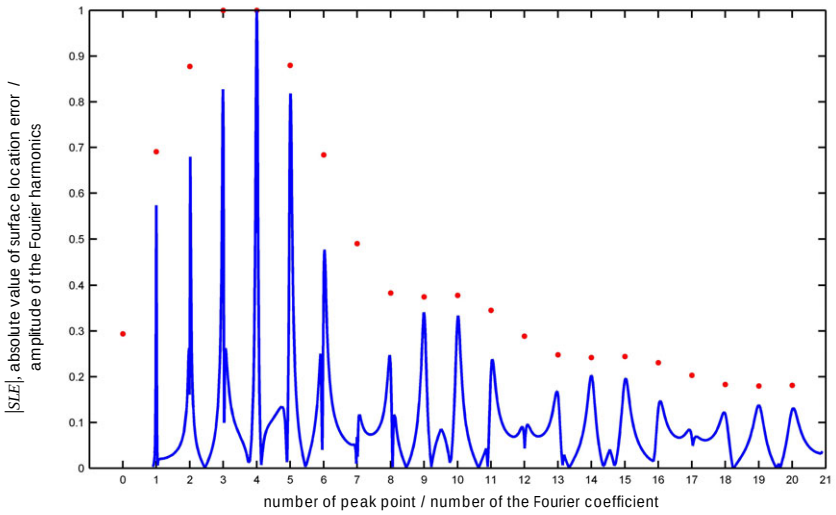

Figure 40: Surface location error plotted against the number of peak points and the coefficients of the Fourier series of the cutting force. The vertical coordinate is the relative value to the maximum. Parameters are $Z = 2$, $w = 1[mm]$, $f_z = 0.1[mm]$, $p \to \infty$, $a_{ep} = 0.1$.

Figure 39 shows that the surface roughness is also higher if we are close to the resonance, but its peak points increase at lower frequencies. This is caused by a similar effect described by the SLE. The surface roughness depends mostly on the curvature of the parts of the edge path what generate the surface. At smaller angular velocity the vibration of the tool centre has a higher frequency compared to the spin frequency of the tool. For this reason more waves can superpose on the path of the edge of the rigid tool over a turn, so the curvature of the edge path increases. This effect is shown figure 41.

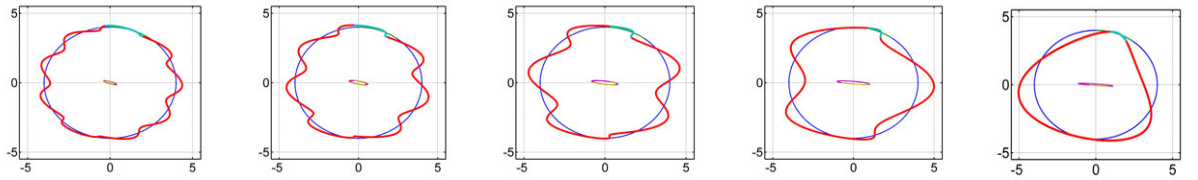

$\Omega = 454[rad/s]$ $\Omega = 568[rad/s]$ $\Omega = 767[rad/s]$ $\Omega = 1135[rad/s]$ $\Omega = 2270[rad/s]$

Figure 41: Edge path in *x*-*y* [mm] plane at different angular velocity.
Parameters are $Z = 2$, $w = 1[mm]$, $f_z = 0.1[mm]$, $p \to \infty$, $a_{ep} = 0.1$.

Figure 42 shows the surface location error and the surface roughness as a function of the axial immersion along $\Omega = 1110[rad/s]$ parameter line, where the system is close to the vibration. Both of the errors are increasing at larger axial immersion. The cutting force is proportional to the axial immersion, so the vibration gets larger at larger axial immersion.

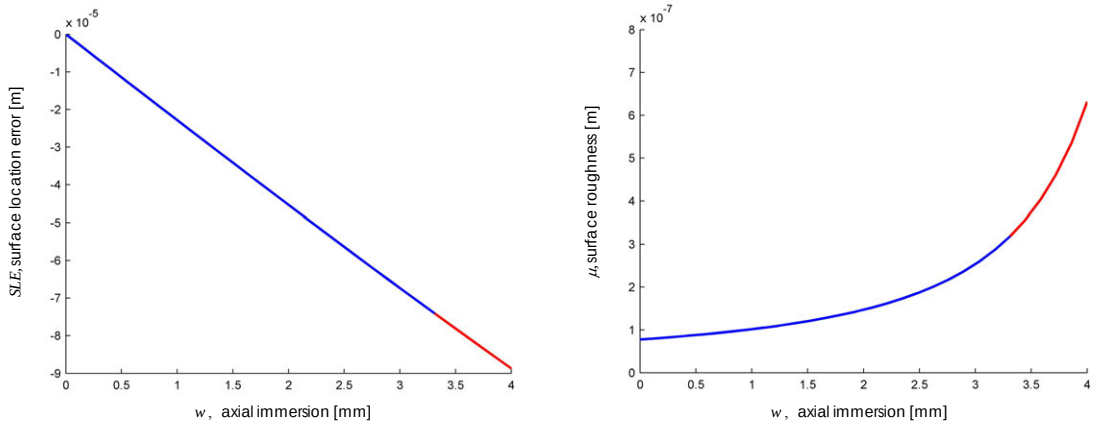

Figure 42: Surface location error and surface roughness as a function of the axial immersion.
Blue lines denote stable process, red lines denote unstable process.
Parameters are $Z = 2$, $\Omega = 1110[rad/s]$, $f_z = 0.05[mm]$, $p \to \infty$, $a_{ep} = 0.1$.

We can check the effect of the feed motion (v) on the surface quality by plotting the surface properties against the feed per tooth (f_z) and fixing all the other parameters (see figure 43). The cutting force is also proportional to the feed per tooth, so changing f_z has a similar influence on SLE as changing the axial immersion. The surface quality is also changed, but in

a different way, since it directly depends on the feed per tooth. (Recall that the stability does not depend on the feed per tooth).

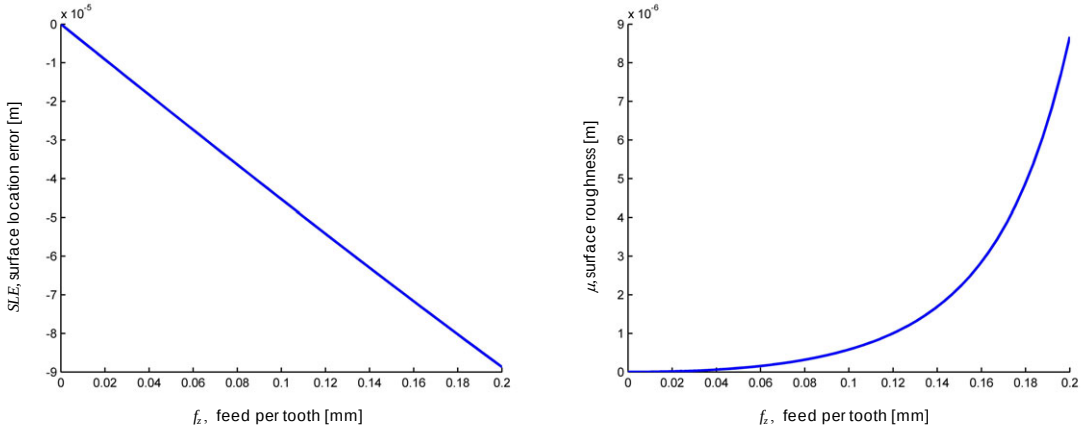

Figure 43: Surface location error, surface roughness for as a function of the feed per tooth. Parameters are $Z = 2$, $\Omega = 1110[rad/s]$, $w_z = 1[mm]$, $p \to \infty$, $a_{ep} = 0.1$.

The surface waviness ($\tilde{\mu}$) is always zero if we use a straight edge tool, but for a tool with a helical edge it is not zero. The surface waviness is of the same order of magnitude as the surface location error if the helix pitch is small enough. In figure 45 we can see that the helix pitch has a great influence on the surface quality. In the case of a constant excitation matrix, so $w\,Z/p$ is close to integer (see equation (105)), there is no tool vibration, but there is a shift due to the constant force. Thus we get the best surface quality in these points.

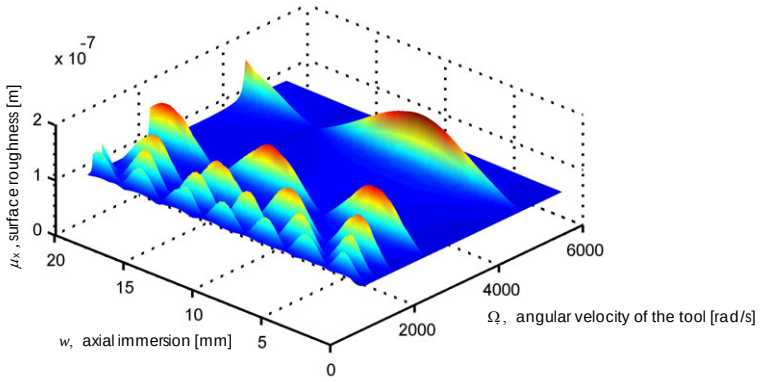

Figure 44: Surface roughness for a helical tool. Parameters are $Z = 4$, $f_z = 0.02[mm]$, $a_{ep} = 0.05$.

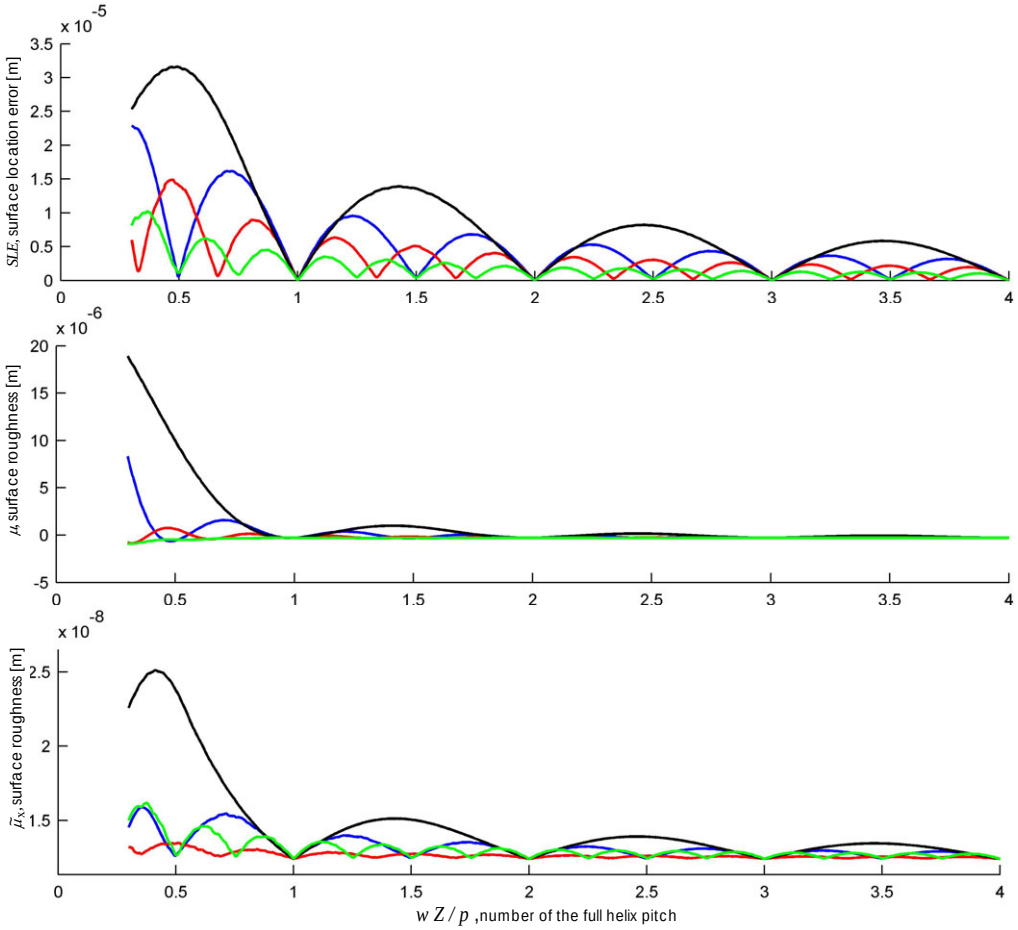

Figure 45: Surface location error, surface roughness and surface waviness as a function of the helix pitch. Parameters are $Z = 4$, $w_z = 2.5[mm]$, $f_z = 0.02[mm]$, $a_{ep} = 0.05$, $\Omega = 1140[rad/s]$ (black line), $\Omega = 570[rad/s]$ (blue line), $\Omega = 380[rad/s]$ (red line), $\Omega = 285[rad/s]$ (green line).

Figure 45 shows that we can achieve the same surface quality between these points. There are as many suitable points in a full helix pitch as the number of the ratio of the natural frequency and the spin frequency of the tool. In these points the duration of the excitation is an integer multiple of the period of the natural vibration of the tool (see figure 46).

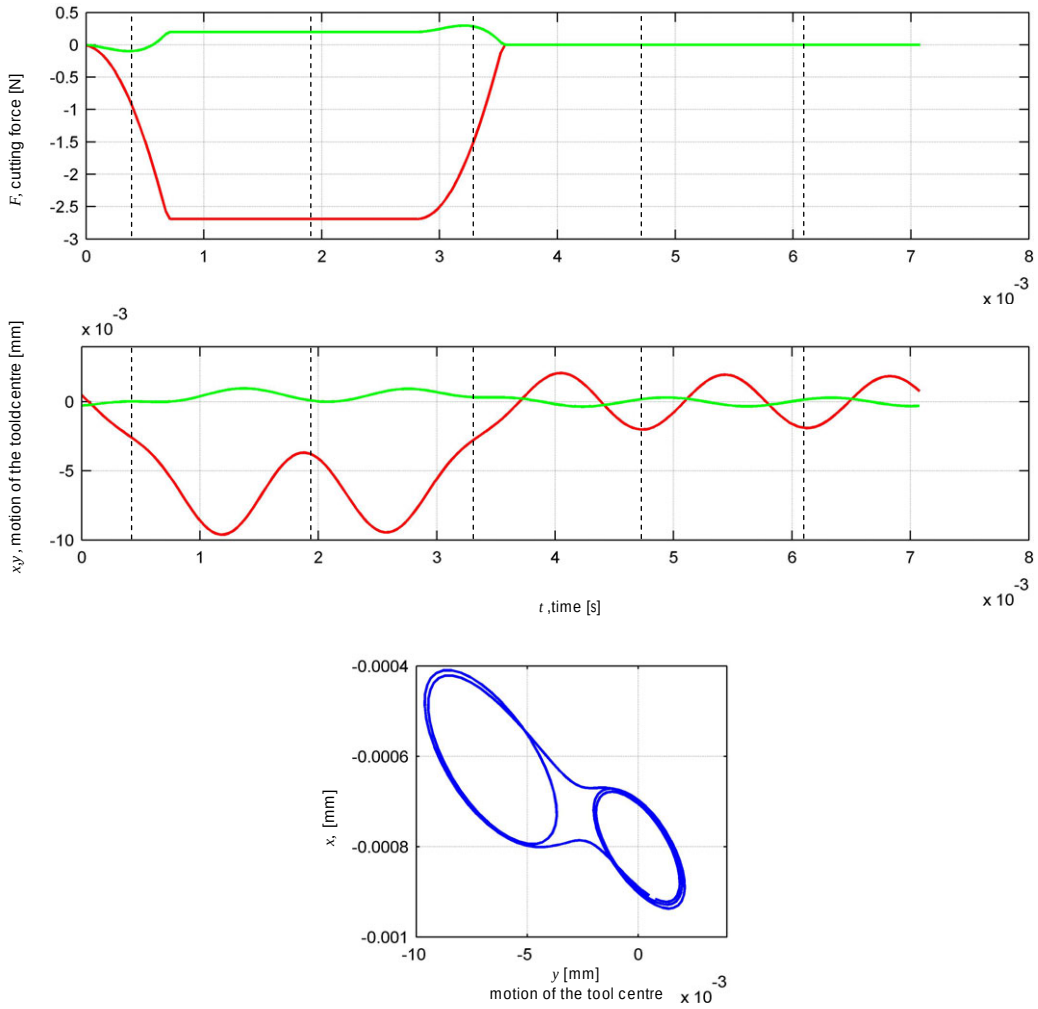

Figure 46: Excitation force and the vibration of the tool centre. Green lines denote the *x* components, red lines denote the *y* components and dash lines denote the period of the natural vibration of the tool. Parameters are $Z = 1$, $\Omega = 888[rad/s]$, $w_z = 1[mm]$, $f_z = 0.05[mm]$, $a_{ep} = 0.1$.

We can see that the position and the velocity of the tool centre stay close to the equilibrium after the cutting phase, due to the small damping of the system. Thus significant vibration cannot be formed. So we get a better surface quality in these points. Figure 45 shows that the surface quality gets better at a smaller helix pitch.

6. Non-linear model

All the above calculations are based on the assumption that the vibration of the tool centre is small. But in some cases, when the system is close to resonance or we use a large axial immersion or feed per tooth, the vibration increases to a level that we can not accept this assumption. In this region we must calculate the chip thickness in a different way.

We can calculate a more precise estimate of chip thickness ($\tilde{h}$) if we consider the velocity of the tool. Usually the chip thickness is defined as the size of the chip along the direction perpendicular to the velocity (see figure 47). In this case we can define an angle between the chip thickness and the side rake of the tool, called the lead angle (κ). The cutting coefficient (k_t) depends on this angle in a highly complicated manner [21]; however we do not deal with this issue here.

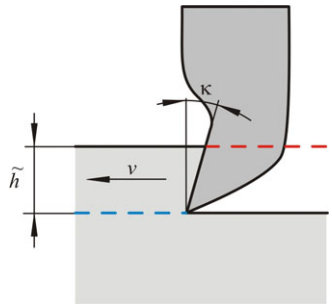

Figure 47: Chip thickness.

In this model we also need some restrictions. We suppose that the second derivative of the edge path is small. In this case the tangent of the tool path can be well approximated by a constant for a short period of time.

A schematic representation of the geometry is shown in figure 48.

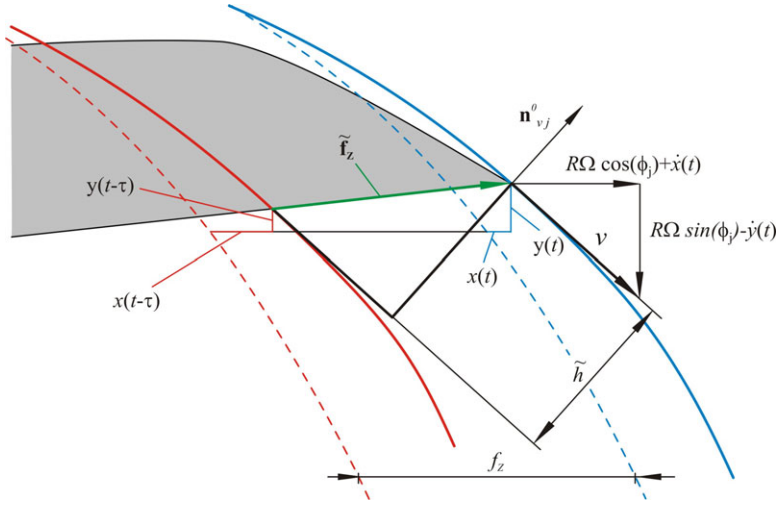

Figure 48: Graphical representation of geometry of the chip thickness.

The chip thickness of the j^{th} tooth ($\tilde{h}_j$) can be calculated as a simple projection of $\tilde{\mathbf{f}}_z$ to $\mathbf{n}^0_{vj}$, which is a unit vector tangent to the velocity of the j^{th} tooth. So

$$\mathbf{n}^0_{vj} = \frac{1}{\sqrt{\left(R\Omega\cos\left(\phi_j(t)\right)+\dot{x}\right)^2+\left(R\Omega\sin\left(\phi_j(t)\right)-\dot{y}\right)^2}}\begin{bmatrix} R\Omega\cos\left(\phi_j(t)\right)+\dot{x} \\ R\Omega\sin\left(\phi_j(t)\right)-\dot{y}\end{bmatrix}, \tag{119}$$

and

$$\tilde{\mathbf{f}}_Z = \begin{bmatrix} f_Z + x(t) - x(t-\tau) \\ y(t) - y(t-\tau)\end{bmatrix}. \tag{120}$$

Using (119) and (120) the chip thickness is given by

$$\begin{aligned}\tilde{h}_j &= \tilde{\mathbf{f}}_Z{}^T \cdot \mathbf{n}^0_{vj} \\ &= \frac{\left(R\Omega\cos\left(\phi_j(t)\right)+\dot{x}\right)\left(f_Z + x(t) - x(t-\tau)\right)+\left(R\Omega\sin\left(\phi_j(t)\right)-\dot{y}\right)\left(y(t)-y(t-\tau)\right)}{\sqrt{\left(R\Omega\cos\left(\phi_j(t)\right)+\dot{x}\right)^2+\left(R\Omega\sin\left(\phi_j(t)\right)-\dot{y}\right)^2}}.\end{aligned} \tag{121}$$

In this model ($\tilde{h}_j$) can be negative so we have to use a step function (H_j) to neglect the negative cutting force, so

$$H_j\left(\tilde{h}_j\right)=\begin{cases}1, & \tilde{h}_j<0\\ 0, & \text{otherwise}.\end{cases} \tag{122}$$

We use the same assumptions for the cutting force as used in section 3.1, that is to say we use a linear force model that has $F_{\mathrm{t}}(0)=0$ (17), where the radial cutting force is proportional to the tangential cutting force (15), (16). Hence we can make the system equation from (6) which is given by

$$\begin{aligned}&\mathbf{M}\ddot{\mathbf{q}}(t)+\mathbf{K}\dot{\mathbf{q}}(t)+\mathbf{S}\mathbf{q}(t)\\&=\sum_{j=0}^{Z-1} w k_{\mathrm{t}}\,\tilde{h}_j(t)g_j\left(\phi_j(t)\right)H_j\left(\tilde{h}_j\right)\begin{bmatrix}-\cos\left(\phi_j(t)\right)-k_{\mathrm{r}}\sin\left(\phi_j(t)\right)\\ \sin\left(\phi_j(t)\right)-k_{\mathrm{r}}\cos\left(\phi_j(t)\right)\end{bmatrix}.\end{aligned} \tag{123}$$

Eq. (123) is a non-linear DDE. In this model the system equation cannot be separated into two parts. We used DDE-BIFTOOL to find the periodic solutions and to check the stability of the solution of system. In this case the stability charts also depend on the feed per tooth. We compute the stability chart for different feed per tooth (see figure 49). We get the same stability chart as for the linear model (described in chapter 3) if we use a very small feed per tooth, because in this case the vibration of the tool is very small. For larger feed per tooth we found a new type of stability loss: a fold bifurcation. In this case an eigenvalue of the Floquet transition matrix ($\mathbf{\Phi}$) crosses the unit circle at the +1 (figure 50).

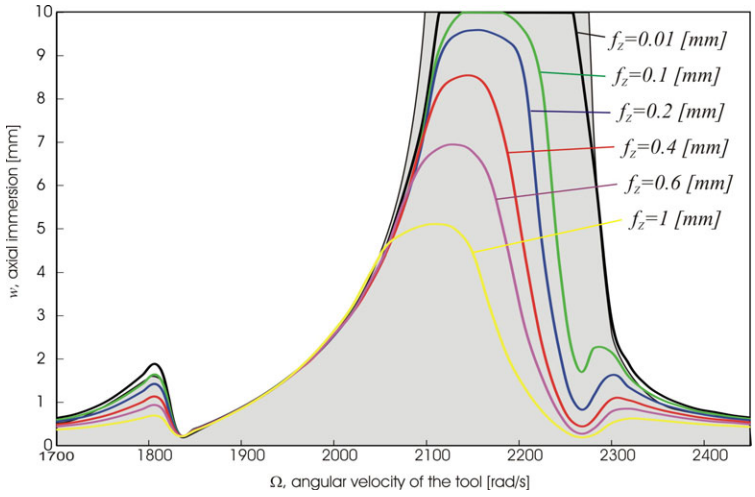

Figure 49: Stability chart for different feed per tooth. Lines denote the stability boundary of the non-linear model, shaded region denote the stabile region of the linear model. Parameters are $Z = 1$, $a_{ep} = 0.1$, $p \to \infty$.

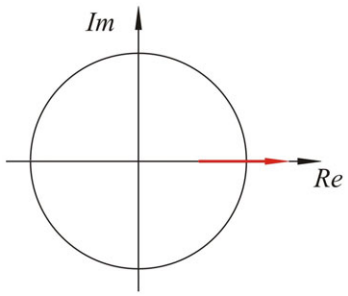

Figure 50: Stability losing by fold bifurcation.

It is not necessary that the unstable vibrations tend to infinity for the non-linear model. For this reason we follow the solution for $\Omega = 2253[rad/s]$. We create a bifurcation diagram by plotting the amplitude of the vibration against the axial immersion (figure 51). We found that the fold bifurcation is a boundary of a bi-stable region.

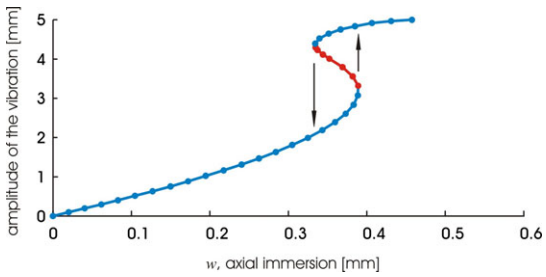

Figure 51: Bifurcation diagram. Blue lines denotes stable periodic solution, red lines denote instable periodic solution. Parameters are $Z =$, $\Omega = 2253[rad/s]$, $f_z = 0.5[mm]$, $a_{ep} = 0.1$.

We can see in figure 49 that this type of bifurcation can occur for even small radial immersion if we are close to resonance. Such behaviour cannot be described with the linear model. Thus we cannot use the simpler linear model in those parameter regions where the amplitude of the vibration is large.

We could use the non-linear model as a better approximation to the linear model, but the non-linear model also has some drawbacks. Firstly two separated step functions (g_j, H_j) are used, but in reality this two functions are coupled.

The second problem is the force model. If the amplitude of the vibration is large, then the variable lead angle (κ) is significant, inconsistent with our assumption of a constant cutting coefficient (k_t).

Thirdly, the teeth can leave the surface and make contact again during one cutting phase. In this case the surface is not formed form the current tooth path. To describe the surface we need to consider more than one time delay. Our model does not take this 'fly over' effect into consideration.

Finally, the Fourth problem is that the model is good only for a tooth path with small curvature.

7. Conclusion

This report has investigated the dynamics of milling, with particular fouls on the milled surface. First we investigated a 2 degree of freedom model with a straight edged tool, to develop our methods and have a comparison for later more complicated models. We determined the system equation for the general case of milling. The equation was separated into two parts, which described the periodic motion of the tool centre and the stability of the system.

We computed the stability chart by using the semi-discretization method. To check our result we also calculated the stability using the Matlab package DDE-BIFTOOL. The results of the two numerical methods fitted very well, so the accuracy of the semi-discretization method was found to be good enough for later use. In the stable region of the stability chart we examined the properties of the transient motion. We found that there are special regions where it dies out much faster.

We then turned to calculating properties of the milled surface. First we calculated the periodic motion of the tool analytically. This analytical solution can be used for real technical parameters of end-milling. We also checked this solution with a numerical time domain simulation, and we showing the problem of the small damping of the system. We used this periodic solution to generate the surface and define two properties to describe the surface quality. The first was the surface location error which is an offset error, between the desired and the milled surface, and the second was the surface roughness, which is the biggest deflection of the milled surface.

We then moved on to considers a helical tool. We began by determining the equations of motion with a helical tool. We calculated the excitation force analytically. This equation was also separated to two parts. We modified our semi-discretization method and solved the first part which described the stability of the system. We found the phenomenon that a flip bifurcation cannot be formed along special parameter lines determined by the helix pitch in the stability chart. The flip bifurcation occurs due to the parametric excitation. For given axial immersion the excitation matrix is time independent, so these parameter lines separate the flip bifurcation islands.

We calculated the periodic motion of the tool centre (the second part of the system equation of the helical model). The analytical method proved be too difficult to use in the general case. For this reason we determined the motion of the tool centre by expanding the excitation as a Fourier series.

Using this solution we generated the motion of the edges. We found that this motion has no regularity in the direction of the axis of the tool (z), despite the fact that the motion is parallel to the x-y plane. Thus the milled surface had to be described as a three dimensional surface. We calculated the properties of the surface with the same parameters as in the straight edged model, as well as defining a new parameter which describes the deflection along the z coordinate: the surface waviness.

We took the modal parameters of a real machine-tool, and the cutting coefficients from realistic material to describe the effect of the parameters.

First we checked the effect of the parameters on the stability chart. We found that large axial immersion can be used at spin speeds, where the ratio of the natural frequency of the system to the angular velocity is close to an integer. This effect derives from the well know 'lobe-structure'.

Our calculations supported the result of practical experiments, that a larger axial immersion can be achieved by using a small radial immersion, and tool with a few teeth. We found that the helix pitch has no great influence on the size of the stable region, but just changes the shape of the boundary lines.

We then checked the effect of the parameters on the surface quality. We found that the advantages that we can use large axial immersion at the above mentioned angular velocities cannot be used in case of straight edged tool, because in this region the surface quality is very poor due to we are very close to resonance.

We found that the surface location error changed almost proportionally to the axial immersion; however the surface quality got significantly worse for increasing axial immersion.

The feed per tooth has the same influence on the surface properties as the axial immersion, but according to the linear model the stability does not depend on this parameter.

Our most important observation was that if we use an appropriate helix pitch, good surface properties can be achieved in the case of resonance angular velocities. We found new

phenomenon that the appropriate helix pitches are not just those where the excitation matrix is time independent (so there is no flip bifurcation), but that there are others equally spaced between them, where the spacing depends on the angular velocity.

We found that large vibrations can occur in some parameter region, so the commonly used approach of the statically chip thickness is no longer valid. Thus we construct a new non-linear model which considers the vibration of the tool. Despite not being an exact model, it showed that new type of behaviour appears in the system such as bistable regions caused by fold bifurcation.

Further aims would be to make an experimental validation of the calculated surface qualities, as well as a more precise model of the chip thickness which considers the effect of the state-dependent delay. We would also investigate the effect of higher modes of the machine-tool in the stability chart.

8. References

[1] T. Insperger, J. Gadišek, M. Kalveram, G. Stépán, K. Weinert, E. Goverkar, Machine tool chatter and surface quality in milling processes, in *Proceedings of ASME International Mechanical Engineering Conference and Exposition*, Anaheim CA, (2004), paper no. IMECE2004-59692 (CD-ROM).

[2] J. Gradišek, E. Govekar, I. Grabec, M. Kalveram, K. Weinert, T. Insperger, G. Stépán, On stability prediction for low radial immersion milling, *Machine Science and Technology*, 9 (2005), 117-130.

[3] T. Insperger, G. Stépán, Semi-discretization method for delayed systems, *International Journal for Numerical Methods in Engineering 55,* (2002) 503-518.

[4] Y. Altintas, E. Budak, Analytical prediction of stability lobes in milling, *Annals of the CIRP* 44 (1) (1995) 357-362.

[5] G. Peigné, H. Paris, D. Brissaud, A model of milled surface generation for timedomain simulation of high speed cutting.

[6] H. M. Shi, S. A. Tobias, Theory of finite amplitude machine tool instability, *International Journal Machine Tool Design & Research, 24.* (1984) No. 1. 45-69

[7] R.P.H. Faassen, N. van de Wouw, J.A.J.Oosterling, H. Nijmeijer, Updated tool path modelling with periodic delay for chatter prediction in milling, *Proceedings of the Fifth Euromech Nonlinear Dynamics Conference, August 7-12, 2005 (ENOC 2005), Eindhoven,* (2005) 1080-1089.

[8] T. Insperger, G. Stépán, J. Turi, State-dependent delay in regenerative turning processes, *Nonlinear Dynamics*, submitted (2005).

[9] R. Szalai, *PDDE-CONT: A continuation and bifurcation software for delay-differential equations* (2005)

[10] K. Engelborghs, T. Lizyanina, G. Samaey, DDE-BIFTOOL v. 2.00 a Matlab package for bifurcation analysis of delay differential equations, *Report TW 330*, (2001)

[11] A.-P. Xu, Y.-X. Qu, D.-W. Zhang, T. Huang, Simulation and experimental investigation of the end milling process considering the cutter flexibility. *Internal Journal of Machine Tool & Manufacture 43* (2003) 283-292

[12] R. Szalai, G. Stépán, Lobes and lenses in the stability chart of interrupted turning, *ASME Journal of Computational and Nonlinear Dynamics*, (2006).

[13] T. Insperger, J. Muñoa, M. Zatarain, G. Peigné, Unstable islands in the stability chart of milling processes Due to the helix angle, preprint (2006).

[14] J. Gradišek, M. Kalveram, K. Weinert, Mechanistic identification os specific force coefficient for general end mill, *Internal Journal of Machine Tool & Manufacture 44* (2004) 401-414

[15] H. Paris, G. Peigné, R. Mayer, Surface shape prediction in high speed milling, *Internal Journal of Machine Tool & Manufacture 44* (2004) 1567-1576

[16] Mitsubishi, Tool news; High Power, Medium, 4 flute YC-MHD; Multi-functional Indexable Cutter APX3000; B007G-B055G (2005)

[17] S. Engin, Y. Altintas, Generalized modelling of milling mechanics and dynamics: Part I – Helical end mills

[18] G. Stépán, The short regenerative effect in machine tool vibrations *Proceedings of 1st Conference on Mechanics* (Praha, 1987), Videopress, Praha 2 (1987), 192-195

[19] J. K. Hale, S. M. V. Lunel, Introduction to functional differential equations, *Applied mathematical sciences*, 99

[20] G. Stépán, *Retarded Dynamical Systems*, Longman, London, (1989)

[21] X.Y. Determination of the cutting force. (1999)

9. Notation

a_e	radial immersion [m]
a_{ep}	dimensionless radial immersion [1]
$\mathbf{A}_i$, $\mathbf{B}_i$	coefficient of the the i^{th} first order ODE in semi-discretization method $\mathbf{B}_i$ belongs to the retarded part
$\mathbf{a}_l, \mathbf{b}_l$	coefficient of the Fourier series of the cutting force
$\mathbf{c}_l, \mathbf{d}_l$	coefficient of the Fourier series of the motion of the tool centre
D	diameter of the tool [m]
$\mathbf{e}(t)$	general variable for the motion of the edge
$\mathbf{e}_{rel}(t)$	general variable for the motion of the edge relative to the surface
$\mathbf{F}$	general force [N]
$\mathbf{F}_j$	force [N]
$\mathbf{F}_{t,j}$, $\mathbf{F}_{r,j}$	tangent and radial components of the force of j^{th} tooth [N]
$\mathbf{f}(t)$	excitation force of the non-delayed system
f_z	feed per tooth [m/tooth]
$g_j(t)$	step function
$h_{j,}, \tilde{h}_j$	chip thickness for linear and non-linear model [m]
$h_{j,stat}$, $h_{j,din}$	static and dynamic chip thickness of the j^{th} tooth [m]
H_j	setp function to neglect the negative force
$\mathbf{K}$	damping matrix [Ns/m]
k_x,k_y	components of the diagonal damping matrix [Ns/m]
k,k_t	cutting coefficients [N/m^2]
$\mathbf{M}$	mass matrix [kg]
m	number of single ODEs in the semi-discretization method
m_x,m_y	components of the diagonal mass matrix [kg]
N_F	number of the terms in the truncated Fourier series
N_{full}	number of the full period
$\mathbf{n}_{vj}^0$	unit vector tangent to the velocity of the j^{th} edge
$\mathbf{P}_i$, $\mathbf{R}_i$	element of $\mathbf{Z}_i$ in semi-discretization method

p	helix pitch
$\mathbf{q}$(t)	the general coordinate of the tool centre $\mathbf{q}(t)=\begin{bmatrix} x_c(t) \\ y_c(t) \end{bmatrix}$ [m]
R	radius of the tool [m]
$\mathbf{S}$	stiffness matrix [N/m]
s_x,s_y	components of the diagonal stiffness matrix [N/m]
$\mathbf{s}(t)$	parametrical graph for surface segment
SLE	surface location error
$\tilde{t}$	relative time coordinate
T_{in}, ϕ_{in}	time, angle when the tooth reaches the surface, start cutting
T_{out}, ϕ_{out}	time, angle when the tooth leaves the surface, finish cutting
T_{cut}, ϕ_{cut}	time, angle length while a tooth cut
T_{fly}, ϕ_{fly}	time, angle length while a tooth does not cut
$\mathbf{T}(\phi_j(t))$	transformation matrix
Δt	Time interval of semi-discretization method [s], and time step of the time domain simulation
$\mathbf{u}(0)$	position and velocity of the tool centre at the beginning of the cutting
$\mathbf{u}(\tilde{t})$	general variable in the shifted time for the first order non-delayed system equation
$\mathbf{u}(t)$	general variable for the motion of the tool centre
$\mathbf{u}_i$	general variable for the i[th] first order ODE in semi-discretization method $\mathbf{u}(t)=\left[\dot{\xi}(t) \quad \dot{\eta}(t) \quad \xi(t) \quad \eta(t)\right]^T$
$\mathbf{v}_k, \mathbf{v}_s, \mathbf{v}_c$	coefficients of the constant, the sin and the cos part of the excitation in the first order non-delayed system equation
$\mathbf{v}_i$	variable for the discreet map in semi-discretization method
v	velocity of feed [m/s]
v_p	speed of the cutting edge [m/s]
w	chip width, axial immersion [m]
$\mathbf{W}(t)$	periodic excitation matrix for the tool with straight edge [N/m]
$\tilde{\mathbf{W}}(t)$	periodic excitation matrix for the tool with helical edge [N/m]
$\overline{\mathbf{W}}$	average of the excitation matrix

$\mathbf{x}(t)$	Solution of the non-delayed part of the system equation $\mathbf{x}(t)=\begin{bmatrix} x(t) \\ y(t) \end{bmatrix}$ [m]
x(t)	horizontal component of the tool centre [m]
y(t)	vertical component of the tool centre [m]
Z	number of teeth [1]
$\mathbf{Z}_i$	coefficient of the discreet map in semi-discretization method
μ	the surface roughness for straight edged tool
μ_x	the surface roughness for helical tool
$\tilde{\mu}$	surface waviness
μ_0	the surface roughness in of the rigid tool and rigid work-piece model
μ_1	the biggest eigenvalue of $\mathbf{\Phi}$
ψ	total arc of the helical edge
$\tilde{\psi}$	reminder arc of the helical edge $\tilde{\psi} \leq 2\pi$
κ	lead angle
Ω	angular velocity of the tool [rad/s]
ϕ_j	angular position of j^{th} tooth [rad]
ϕ_j'	cyclical coordinate for the angular position of j^{th} tooth [rad]
$\mathbf{\Phi}$	Floquet transition matrix
$\xi(t)$	Solution of the delayed part of the system equation $\xi(t)=\begin{bmatrix} \xi(t) \\ \eta(t) \end{bmatrix}$